https://doi.org/10.1016/j.applthermaleng.2018.08.038

Cross-Impingement and Combustion of Sprays in High-Pressure Chamber and Opposed-piston Compression Ignition Engine

Zhenyu Zhang[a], Peng Zhang[a*]

[a] *Department of Mechanical Engineering, The Hong Kong Polytechnic University, Hong Kong, PR. China*

Abstract: Spray cross-impingement in a high-pressure chamber (10-30 atm) was studied experimentally, the results being compared to the spray opposed-impingement. The comparison was subsequently extended to the spray combustion in a model opposed-piston compression ignition engine. To account for the ambient pressure effects in collision outcomes, a recently proposed pressure-dependent droplet collision model was implemented in the KIVA-3V computer program for simulating the experiments. Compared with the widely used Estrade et al.'s and O'Rourke's models, the pressure-dependent model produces satisfactory predictions to spray characteristics. The uncertainty of the kinetic energy recovery coefficient, which affects the post-collision characteristics of bouncing droplets, was found to cause insignificant difference in model predictions. In the high-pressure chamber, droplet collisions in cross-impingement occur earlier than those in the opposed-impingement and result in more coalescence, consequently producing larger droplet sizes. With increasing the ambient pressure, the increasing tendency of droplet bouncing diminishes the difference of these two spray impingements. In the model OPCI, the presence of strong swirling flow deflects sprays from impingement and therefore the opposed-impingement shows slightly better combustion performance by producing more spatially uniform droplet distribution. However, the spray cross-impingement enhances droplet collision hence promotes atomization in the absence of swirling flow.

* Corresponding author
E-mail pengzhang.zhang@polyu.edu.hk.
Fax: (852)23654703 Tel: (852)27666664

Keywords: Spray impingement; Droplet bouncing; Kinetic energy recovery coefficient; High-pressure chamber; Opposed-piston compression ignition.

1. Introduction

In recent years, there are rekindled interests in opposed-piston compression ignition (referred to as OPCI hereinafter) engines [1-12], where cylinder head is absent and fuel injectors are mounted on the cylinder liner. In order to sufficiently utilize the in-cylinder air, two fuel injectors are usually so oriented that their sprays tend to impinge with each other, rendering binary droplet collision a frequent event in cylinder. It is evident that the collision outcomes, such as droplet bouncing, coalescence and separation, can substantially influence the size and velocity distributions of droplets and in turn the subsequent combustion and emission [13].

Earlier experiment [14] on water droplet collision under atmospheric environment shows that the collision outcomes are either coalescence or stretching separation, depending on the collision Weber number, $We = 2\rho_l U^2 R_s/\sigma$, the impact parameter, $B = X/(R_s + R_L)$, and the size ratio $\Delta = R_s/R_L$, where ρ_l is the liquid density, U is the relative velocity of the colliding droplets, σ is the surface tension coefficient, X is the projection of the distance between the mass centers of the droplets in the direction normal to the relative velocity, R_s and R_L are the radii of smaller and larger droplets, respectively. This result was subsequently adopted by O'Rourke [15] in developing his droplet collision model, which is implemented in the widely used KIVA [16] computer program for the Eulerian-Lagrangian simulation of spray combustion.

By recognizing that liquid alkanes are more relevant to the hydrocarbon fuel, Jiang et al.'s [17] and Qian and Law's [18] experiments on droplet collision of liquid alkanes, for the first time, identify droplet bouncing as a commonly encountered collision outcome, which is however seldom seen for water droplet collision under atmospheric pressure and hence absent in O'Rourke's [15] collision model. Duo to its incomplete description on the main collision outcomes of hydrocarbon fuel droplet, the over-simplified O'Rourke's droplet collision model was subsequently improved by a number of models, which has been summarized in a few reviews [19-22]. Majority of the models aim to estimate the collision probability [23, 24], to reproduce the complex collision outcomes [19, 20, 22, 25-30], and to predict the post-collision characteristics of droplets [31]. However, the influence

of ambient pressure on droplet collision has never been concerned.

Although Qian and Law [18] experimentally confirmed that droplet bouncing is promoted by increasing ambient pressure and that the underlying physics has been theoretically delineated by Zhang and Law [32], no modelling effort was made previously to account for the influence of ambient pressure until very recently Zhang et al. [22] proposed a practically simple pressure-dependent droplet collision model based on the experiment results of Qian and Law [18] and the theoretical analysis of Zhang and Law [32]. Compared with the previous models, for example Estrade et al.'s [33] bouncing-coalescence model, which does not account for the fact that increasing of ambient pressure promotes droplet bouncing, the pressure-dependent model produces better predictions to the available experimental data [34] on impinging spray characteristic, especially under high ambient pressures.

Zhang et al. [35] also applied the pressure-dependent model to study spray impingement and combustion in a model OPCI engine, where two oppositely-oriented multiple-nozzle injectors with C_2 symmetry were investigated and optimized. Although the model again shows better performance than others in predicting the spray characteristics under high pressures, its advantage is not easily perceived when the in-cylinder swirling flow is sufficiently strong to deflect the inter-injector sprays (from two different injectors) from being impinged. The impingement of intra-injector spray (from two different nozzles of the same injector) is always presented and enhanced by the swirling flow, but it is not the same effective as the inter-injector spray impingement in promoting droplet collisions.

The present study was motivated by exploring new spray setup to promote inter-injector spray impingement, which has been found to enhance fuel atomization and subsequent fuel/air mixture and combustion [34, 36-38]. Recognizing that the in-cylinder swirl suppresses the inter-injector spray impingement from two opposed-oriented injectors, we audaciously proposed a spray setup with perpendicularly oriented injectors, which may result in the spray cross-impingement. The present study aims to experimentally and numerically investigate spray cross-impingement in a high-

pressure chamber and in a model OPCI engine, the results were compared with that of opposed-impingement. In the following text, we shall describe the experimental and numerical specifications of the cross-impingement sprays, in Section 2. The results and discussion of spray cross- and opposed-impingement in high-pressure chamber, in Section 3, followed by the spray combustion of cross- and opposed-impingement in a model OPCI, in Section 4.

2. Experimental Specifications and Numerical Methods

2.1 Spray layout of cross- and opposed-impingement

Figure 1 shows the schematic of spray cross- and opposed-impingement layouts. It should be noted that, the present cross-impingement spray layout was developed based on Zhao et al.'s [11] spray patterns, while the opposed-impingement layout was developed according to Hofbauer's [2] optimized results. The cross-impingement was developed to promote spray impingement and atomization, while opposed-impingement was designed to generate more uniform droplet distribution in the combustion chamber.

For the cross-impingement shown in Figure 1(a), each injector consists of three nozzles, No. 1 – No. 3 refers to one injector while No. 4 – No. 6 refers to the other one. No. 2 and No. 5 are on the Z=0 plane, No. 2 and No. 5, projections of No. 1 and No. 4 (similarly, No. 3 and No. 6) on Z=0 plane are symmetrical with respect to the plane X=Y. No. 1 and No. 3 (similarly, No. 4 and No. 6) are on the same plane with an angle of 3° respect to X=0 plane. The angles between No. 1 – No. 3 and the Y-axis on Z=0 plane are 45°, 5° and 30°, respectively. Similarly, angles between No. 4 – No. 6 and the X-axis on Z=0 plane are also 45°, 5° and 30°, respectively.

For the opposed-impingement shown in Figure 1(b), No. 1 – No. 3 are the same to that in cross-impingement, the opposed-impingement possesses the C_2 symmetry so that that No. 1 and No. 4 sprays (similarly, No. 2 and No. 5, and No. 3 and No. 6) can interchange their positions by rotating for 180° with respect to the Z=0 axis.

2.2 Experimental Apparatus

The experiment in the present paper contains two synergetic parts, which serve to validate the simulation for the non-reacting and isothermal sprays in constant-volume chamber and then for the reacting and variable-temperature sprays in an OPCI model engine.

The simplest the first, we investigated the non-reacting impinging sprays in a constant-volume chamber without heating; the temperature in the chamber was constant at 298K. The objective of the non-reacting impinging spray in the constant volume vessel is to validate the adopted pressure-dependent droplet collision model. Isothermal chamber suppresses droplet evaporation so that liquid droplets in the chamber have longer residence time, which facilitates the comparison of the predictions from different droplet collision models (i.e., O'Rourke's [16] model, Estrade et al.'s [33] model and the pressure-dependent model [22]). It is extremely difficult to experimentally measure the spray evolution in the operating engine, although it definitely merits future study. Subsequently, we extended the investigation to the combustion of cross-impingement impinging sprays in an opposed-piston compression ignition (OPCI) engine, where the moving pistons make the chamber flow statistically unsteady. The combustion temperature, varying with the crank angle, is similar to that in real engines.

Schematics of the experimental apparatus for non-reacting cross- and opposed-impingement sprays in a high-pressure chamber and cross-impinging spray combustion in a model OPCI engine are shown in Figure 2(a) and 2(b). A complete description of the experimental apparatus for impinging sprays can be found in our previous publication [22], so only a brief description of the experimental set up will be given here. For non-reacting spray impingement, time-resolved shadowgraph images in the chamber (1) with two opposed glass windows were taken by a Fastcam SA4 camera (10000 fps) (2) combined with a stroboscope (3). The chamber was filled with pure nitrogen with varying pressure at 10 atm, 20 atm, and 30 atm, respectively. A Bosch CP1H3 common rail system (4) was adopted for fuel injection. The injection pressure was 160 MPa and the injection duration was 1.5 ms with total of 90 mg/cycle liquid diesel was injected into the chamber

by two injectors, simultaneously.

The model OPCI (5) with 100 mm in bore and 110 mm in stroke for each piston is schematized in Figure 2(b). Similarly, the detailed description of OPCI working principle can be found in one of our previous publication [35]. For a briefly introduce, the engine prototype has two cylinders and a total displacement of 3.4 liters with the rated speed is 2100 rpm. Each cylinder contains two oppositely moving pistons, namely, intake piston and exhaust piston, respectively. Thus, cylinder head is absent and fuel injectors can only be installed on the cylinder liner. The OPCI engine employs a port-to-port uniflow scavenging system for gas exchange, and the port opening and closing are controlled by corresponding pistons. In this study, the exhaust ports open at 100° ATDC (after top dead center) and close at 113° BTDC (before top dead center); the intake ports open at 116° ATDC and close at 110° BTDC. Engine power and torque were measured by an electrical dynamometer. A Kistler-6056A cylinder pressure transducer (6) together with a Kistler 2614B crank angle sensor (7) were used to collect the cylinder pressure data with a crank angle interval of 0.2° CA and for 200 engine cycles. The pressure data was used to estimate heat release rate by using Krieger and Borman's [39] method. Intake pressure and exhaust pressure were measured by a Kistler 4005B pressure sensor (8) and a Kistler 4049A pressure senor (9), respectively. The measured intake and exhaust pressure were adopted to set up the numerical simulation, while the measured cylinder pressure was used to estimate heat release rate and validate the simulation results.

2.3 Numerical Methodology

Reynolds Average Navier-Stokes (RANS) calculations were adopted in the present study by using the widely used computer program KIVA-3V. The standard k-ε model [40] was adopted for turbulence modelling and the SIMPLEC method [15] for velocity-pressure coupling. The TAB model [41] and Spalding model [42] were used to account for the subsequent droplet breakup and evaporation, respectively. The Arrhenius law [16] was used to calculate chemical reaction rate constants. The pressure-dependent droplet collision model, which accounts for the propensity of droplet bouncing with increasing ambient pressure and proposed by Zhang et al. [22], was adopted to

account for droplet collision. Simultaneously, the widely used O'Rourke's [15] and Estrade et al.'s [33] droplet collision model were also used to calculate non-reaction spray characteristic for a comparison.

Figure 3 illustrates the *We-B* regime nomogram (for n-hexadecane droplets) for Zhang et al.'s [22], Estrade et al.'s [33] and O'Rourke's [15] model, respectively. For Zhang et al.'s model shown in Figure 3(a), to account for that bouncing is promoted by increasing the ambient pressure, Estrade et al.'s bouncing criterion was modified by adding a pressure-dependent factor $g(p)$ determined by fitting Qian and Law's [18] experimental data, given by

$$We < We_{cr}(p,\Delta,B) = g(p)\cdot We_{cr}(1,1,0)\frac{\Delta(1+\Delta^2)(4\Theta'-12)}{2.8\chi_1\{\cos[\sin^{-1}(B)]\}^2} \quad (1)$$

with $g(p) = 0.25p + 0.75$. Here, $We_{cr}(p,\Delta,B)$ is the bouncing-coalescence transition Weber number at various p, Δ, and B. $We_{cr}(1,1,0) = 15.5$ for n-hexadecane was adopted in the present study [43]. The Estrade et al.'s model shown in Figure 3(b) was developed according to the experimental observation on ethanol droplet collision [33] under atmospheric pressure, only bouncing and coalescence are considered in this model, and the bouncing criterion can be written as

$$We < \frac{\Delta(1+\Delta^2)(4\Theta'-12)}{\chi_1\{\cos[\sin^{-1}(B)]\}^2} \quad (2)$$

the RHS of Eq.(2) is equal to 2.8 for $\Delta = 1.0$ and $B = 0$, corresponding to the constant term in the denominator of Eq.(1). In Eq.(1) and (2), the shape factor $\Theta' = 3.351$ and χ_1 is determined by $\chi_1 = 1 - 0.25(1+\tau)(2-\tau)^2$ if $(r_1 + r_2)(1 - B) > r_1$, otherwise, $\chi_1 = 0.25(3-\tau)\tau^2$, where $\tau = (1 - B)(1 + \Delta)$.

Unlike Estrade et al.'s [33] and Qian and Law's [18] experiment on hydrocarbon droplets, O'Rourke's [15] model was developed by Brazier-Smith et al.'s [14] experimental observation on water droplet collision, hence droplet bouncing is absent but involving in stretching separation without fragmentation (a.k.a. grazing), as shown in Figure 3(c). The stretching separation criterion

can be written as

$$B > B_{cr} = \sqrt{\min\{1.0,\ 2.4(\Delta^{-3} - 2.4\Delta^{-2} + 2.7\Delta^{-1})/We\}} \tag{3}$$

Furthermore, it is noted that the narrow bouncing regime in Estrade et al.'s model tends to predict more droplet coalescence and therefore larger droplet size than the other two models.

Because the boundary between bouncing and coalescence right shifts to higher Weber number with ambient pressure increasing, droplet bouncing is considered as the primary collision outcome for prevalent droplet size and velocity [18]. Recognizing that droplet bouncing or grazing are inelastic, the post-collision velocity can be determined by

$$u_{n,i} = \frac{u_i R_i^3 + u_j R_j^3 + R_j^3 (u_i - u_j)\sqrt{1 - f_E}}{R_i^3 + R_j^3} \tag{4}$$

here, u is the droplet velocity, the subscript n denotes the droplet after bouncing, i and j refer to two interacting droplets, f_E is the kinetic energy dissipation factor and $1 - f_E$ can be regard as the kinetic energy recovery coefficient, which shall be discussed in Section 3.3.

A cubic computational domain of (100 mm)^3 and a uniform Cartesian mesh with 125,000 grid cells of (2 mm)^3 were used to simulate spray cross-impingement and opposed-impingement in the high-pressure chamber, as shown in Figure 4(a). It should be noted that, the mesh independence study has been done in our previous publications [22]. For a briefly summary, the evolution of the predicted spray penetration length with time of Chiba et al.'s [34] experiment for six different meshes from the coarsest $5 \times 5 \times 5$ mm^3 to the finest $1 \times 1 \times 1$ mm^3. The calculated results show a significant dependence on the cell size coarser than $2 \times 2 \times 2$ mm^3, beyond which the grid-dependence is substantially reduced. Similar cell size also adopted by Kim et al. [21] for their impinging spray simulation. Boundary effects in this calculation can be neglected in the present problem because the domain size is much larger than the size of the sprays and the penetration length. Consequently, the domain boundaries can be simply set as isothermal walls of 298 K and with the nonslip conditions for velocity.

In order to investigated spray combustion characteristic in the OPCI with varying volume and ambient pressure. Spray combustion of cross- and opposed-impingement in the OPCI engine was simulated by using a full-scale three-dimensional dynamic mesh with intake ports and exhaust ports, containing 200615 cells at BDC (bottom dead center) and 32748 cells at TDC (top dead center) after rezone, as shown in Figure 4(b). Intake port was cut into an angle of 20° so as to generate in-cylinder swirl. Liquid diesel was injected into the combustion chamber in the form of droplet parcels. In the Eulerian-Lagrangian simulation, each parcel usually represents many droplets. In this study we assumed the parcel number density is 1000 parcels/mg for both non-reaction spray calculation and spray combustion simulation in the OPCI engine. The full cycle calculation starts at 100° ATDC and ends at 80° BTDC. Initial and boundary conditions, such as intake pressure and temperature, exhaust pressure and temperature, were set according to the experimental data, to be elucidated in the following text. The mesh independence studies on the adopted dynamic mesh also can be found in one of our previous publication [35], and will not repeat in this paper.

Spray layouts for cross- and opposed-impingement were set up according to the experimental conditions, which has been discussed in the Section 2.1. Non-reaction spray characteristics for cross- and opposed-impingement in the constant volume chamber were calculated and a typical run takes about half an hour on an Inter Xeon E5 2692 central processing unit (CPU), while a typical run of full engine cycle for cross- or opposed-impingement combustion takes around 48 CPU hours.

3. Spray cross-impingement in high-pressure chamber

3.1 Experimental and Numerical Shadowgraph Images

Figure 5 shows the impinging spray shadowgraphs at selected time instants under different ambient pressures. The numerical shadowgraph was obtained by taking the second-order derivative of density in the domain. A complete set of experimental and simulation results of spray cross-impingement during the entire process can be found in Fig. S1-Fig. S3 in the Supplemental Material. Figure 5(a) shows the spray cross-impingement at 10 atm. From injection time (i.e., t =0 ms) to t =

0.5 ms when the spray impingement is about to occur, no significant difference between experimental and simulation shadowgraphs can be observed for all the droplet collision models. This is because droplets in the early stage are dominated by aerodynamic deceleration and breakup. In the later stage after t = 0.5 ms, droplet collision become more frequent, but only slight difference among the predictions of the three models can be seen. This is because the aerodynamic deceleration in the gas chamber of 10 atm is insufficiently strong so that the collision *We*s are mostly large enough to affect droplet coalescence. It is evident from Figure 3 that all the models show no significant difference in predicting droplet coalescence at sufficiently large *We* and small *B*.

Figure 5(b) shows the spray cross-impingement at 20 atm. For the same reason stated above, only slight difference among three model predictions can be observed before spray impingement is about to occur by t =1.0 ms. After spray impingement starts, Zhang et al.'s model predicts more droplet parcels than other two models do, because it predicts higher transition *We* for droplet coalescence at increased pressure and therefore more bouncing droplets with unchanged droplet size and reduced inertia (due to inelastic collisions to be discussed in Section 3.3). It is also seen that Estrade et al.'s and O'Rourke's model predict multi-tips spray shape, probably due to the over-predicted droplet sizes and inertia and hence larger shadow regions, but this prediction is not verified by either experimental shadowgraphs or the prediction of Zhang et al.'s model.

Figure 5(c) shows the spray cross-impingement at 30 atm. For comparison, the spray opposed-impingement at 30 atm is also shown in Figure 5(d). It should be noted that, spray opposed-impingement results has been studied in one our previous publication [22]. Owing to its correctly accounting for the pressure-dependence of droplet collision, Zhang et al.'s model predicts results more similar to the experimental images in both cases. Spray impingement (between No. 3 and No. 6 sprays) occurs earlier in Figure 5(c) at around t =1.0 ms, when the spray impingement in Figure 5(d) has not yet happened. It is also seen that the spray opposed-impingement seems to produce more spatially uniform distribution of droplets, which spread out in the chamber center. These spray characteristics may influence combustion characteristics in the OPCI engine, to be discussed in

Section 4.

3.2 Quantitative Comparison of Experiment and Simulation

A grayscale level analysis [22, 44] of shadowgraph images was adopted in the present study for quantitative comparison of different droplet collision models. The time-dependent ratio $r_d = N_d(t \mid G < G_{low})/N_t$ was defined as an indicator of spray spread based on the physical understanding that, in the gray-scale shadowgraph images of impinging spray, the dark areas represent either the droplets or the opaque gaseous species and have the grayscale levels (G=0 for the darkest and G=256 for the brightest) below a threshold value G_{low}. Consequently, $N_d(t \mid G < G_{low})$ is the pixels number in the image with the grayscale level less than G_{low} at the time instant t, and N_t is the total pixels number in the shadowgraph image at the same time instant. Figure 6 shows the evolution of r_d calculated from the experimental and numerical shadowgraphs for different G_{low}. Although all the predictions show good agreement with the experimental results for spray impingement before fuel injection ends, the predicted r_d slightly differ between the models, and Zhang et al.'s model produces increasingly better predictions with increasing pressure. However, moderate discrepancies can be found for the long-time behaviors of droplets after fuel injection ends, and may be attributed to the computational and model uncertainties associated with droplet breakup and vaporization, which become increasingly dominant processes with time. It is also observed that, numerical simulation slightly over-predicts r_d, probably due to the uncertainty of kinetic energy recovery coefficient f_E, to be discussed in the following section.

For further quantitative comparison, the predicted Sauter mean diameters (SMD) which were calculated by averaging the entire droplet diameter in the calculation domain are shown in Figure 7. Note that the experimental data is absent in this comparison because it is difficult to measure the overall SMD in the experiment by counting all the droplet sizes in the chamber. As anticipated, Zhang et al.'s model predicts smaller SMD than others, and the the difference among different model predictions increases with the ambient pressure. This is because Zhang et al.'s model predicts increasingly larger transition We for droplet coalescence with increasing ambient pressure and

consequently more droplet bouncing. The propensity of droplet bouncing at increased ambient pressure is further enhanced by the increased aerodynamic deceleration of droplets, which effect more collisions with smaller *We*s. These results on SMD can be used to explain the discrepancies in r_d among different droplet collision models: Estrade et al.'s and O'Rouke's models tend to over-predict the likelihood of droplet coalescence and hence result in larger droplet size and spreading.

Figure 7 also compares the spray cross-impingement and opposed-impingement for the SMDs predicted by Zhang et al.'s model. It is seen that the spray opposed-impingement has significantly smaller SMD at 10 atm than cross-impingement does, but the discrepancy declines at 20 atm and almost disappears at 30 atm. This can be understood by noting that the cross-impingement occurs earlier and results in more collisions with large *We*s to effect coalescence. With increasing the pressure, the increasing tendency of droplet bouncing diminishes the difference of these two spray impingements.

3.3 Influence and Uncertainty of Kinetic Energy Recovery Coefficient

The kinetic energy recovery coefficient is a key parameter in modelling post-collision characteristics of bouncing droplets, and is defined by O'Rourke [15] as $1 - f_E$, where f_E is the kinetic dissipation rate after bouncing. The determination of f_E entails either experimentally measuring the velocity changes during each collision or computationally tracking droplet interface and internal flow, both of which are beyond the scope of the present study. Recently, Zhang and Zhang [31] numerically simulated the kinetic energy recovery of bouncing droplets after inelastic head-on collision. However, employing their results in the present simulation is premature because the influence of ambient pressure and impact parameter remains unsolved.

To investigate the influence of the uncertainty of f_E on the present simulation, f_E was varied from elastic collision ($f_E = 0$) to totally inelastic collision ($f_E = 1.0$). Figure 8 shows the predictions of r_d and SMD for different f_E. It is seen that r_d and SMD decreases with increasing f_E. This can be understood by recognizing that a larger f_E means a smaller post-collision droplet velocity,

which results in a lower *We* for the subsequent collision and in turn increase the trend of droplet bouncing without size growth. Correlation between f_E with various collision parameters merits future studies on the fundamental phenomena of binary droplet collisions.

4. Spray Cross-impingement and Combustion in OPCI

It is seen above that the spray cross-impingement promotes droplet collision and spray atomization, and hence holds potential of enhancing combustion efficiency. Nevertheless, the spray cross-impingement setup also results in the spatially asymmetric droplet distribution in the combustion chamber and therefore may reduce combustion efficiency [2, 3]. Thus, we compared the spray combustion characteristics between cross- and opposed-impingement with and without swirl in the model OPCI, as shown in Figure 9. Figure 9(a)-(c) show the simulation results at engine speed of 2100 rpm and under 50% load. The simulation results of cross-impingement are validated by the experimental results for cylinder pressure and estimated heat release rate. Figure 9(d)-(f) extend the comparison to the same engine speed but under 100% load; Figure 9(g)-(i) to the same operating condition but without in-cylinder swirl. It should be noted that, in-cylinder swirl was generated by cutting intake port into an angle of 20°. For non-swirl case, this angle was set as 0° in the dynamic mesh. Intake temperature was set as 325 K; intake pressure was 1.2 bar and 1.6 bar for 50% and 100% load, respectively. Full engine cycle was calculated for each case, the calculation starts at 100° ATDC and ends at 80° BTDC.

4.1 Cylinder pressure and estimated heat release rate

Figures 9 (a), (d) and (g) show the in-cylinder pressure (*p*, left Y-axis) and the heat release rate (HR, right Y-axis) at different loads. Experiment cylinder pressure and the estimated heat release rate of cross-impingement spray combustion for 50% load are shown in Figure 9(a) to validate the numerical platform. SOI and EOI denote the start and end of injection. Fuel injection starts at -5° ATDC and ends at 12° ATDC for 50% load, and starts at -8° ATDC and ends at 13° ATDC for 100% loads. Good agreement between experiment and simulation for cylinder pressure *p* can be seen

in Figure 9(a), and the peak value of calculated heat release rate is slightly higher than estimated heat release by using Krieger and Borman's [39] approximation method, probably due to the experimental errors in pressure measurement and the computational uncertainties associated with simplified models for fuel vaporization and combustion. It is also interesting to observe that opposed-impingement produces a higher peak heat release rate and p than cross-impingement does either for the cases with 50% load and 100% load and with swirling flow. However, cross-impingement predicts moderately higher peak heat release rate and p for the case without swirling flow. These results accord with previous findings [35] and our hypothesis stated above that the presence of strong swirling flow deflects sprays from impingement and therefore the opposed-impingement spray setup shows better combustion performance by producing more spatially uniform droplets, as shown in Figure 10(a). In the absence of swirling flow, the influence of spray impingement in enhancing droplet collisions is more prominent for the cross-impingement spray setup, shown in Figure 10(b). More detailed explanations are as follows.

4.2 Evaporation and fuel/air mixture

To explain the above observations, we calculated a time-dependent ratio, $A_{\mathrm{d}} = N_{\mathrm{p}}(t)\mathrm{SMD}^2(t)/N_{\mathrm{p}}(0)\mathrm{SMD}^2(0)$, where $N_{\mathrm{p}}(0)$ and $\mathrm{SMD}(0)$ are the initial parcel number and SMD of droplets, as an indicator of total droplet surface area. Figures 9(b), (e) and (h) show the evolutions of A_{d} (left Y-axis) and premixed fuel mass (m_p, right Y-axis). For 50% load with in-cylinder swirl, no significant difference can be observed on A_{d} and hence on m_p, because fewer fuel droplets were injected into combustion chamber, leading to infrequent droplet collision. With the engine load is increased to 100%, opposed-impingement produces significant higher A_{d} around 2° ATDC and hence the higher premixed fuel mass. By contrast, the non-swirl case shows an opposite tend in that cross-impingement produces higher A_{d} and hence m_p, as shown in Figure 9(h). This also can be used to explain why cross-impingement predicts smaller peak value of heat release rate in the swirl cases but higher peak value in the non-swirl case.

4.3 Droplet size and number density

Figure 9(c), (f) and (i) show the evolutions of the droplet size (SMD, left Y-axis) and the parcel number (N_p, right Y-axis) for different loads. Following the previous study [35], we assumed the initial droplet number density is 1000 parcels/mg. For the same reason stated above, there is no significant difference between two spray setups for 50% load. Larger SMD and lower N_p after TDC can be seen at 100% load in the swirl case, implying that cross-impingement causes more collisions with higher Weber numbers and hence more coalescence, as shown in Figure 9(f). However, for the non-swirl case shown in Figure 9(i), due to the high collision frequency and kinetic energy dissipation, cross-impingement produces more droplet bouncing hence smaller SMD and higher N_p, as explained in the Section 3.3. To the end, although cross-impingement promotes spray atomization, the effects of in-cylinder swirl in impinging-spray combustion are significant by changing in-cylinder gas motion and fuel droplet distribution.

4.4 Engine-indicated thermal efficiency

To facilitate the comparison of spray combustion characteristic in the OPCI between cross- and opposed-impingement, Figure 11 compares the engine-indicated thermal efficiency η_i for different cases corresponding to the Figure 9. The efficiency η_i is defined by [45]

$$\eta_i = \frac{\oint pdV}{m_f Q_{LHV}} \tag{5}$$

where p is the predicted cylinder pressure, V is the engine displacement volume, m_f is the total fuel injection quantity per cycle, and Q_{LHV} is the low heating value of the fuel.

It is seen from Figure 11 that, the opposed-impingement produces significantly higher η_i than does the cross-impingement for both the case of 50% load and that of 100% load with swirling flow. However, the cross-impingement produces moderately higher η_i for the case without swirl. This again can be explained by that strong swirl flow deflects sprays from impingement and η_i is dominated by the uniform extent of droplet distribution. As discussed in Figure 5, the opposed-

impingement produces more uniform mixture hence higher η_i. However, the cross-impingement enhances spray atomization, which dominates η_i under the condition of non-swirl flow.

5. Concluding remarks

An experimental and numerical study was conducted on spray cross-impingement in the high-pressure chamber at 10-30 atm, and in the model OPCI engine, the results being compared to the spray opposed-impingement. The KIVA-3V simulation with the pressure-dependent droplet collision model [22] predicts satisfactorily the spray impingement and combustion in high ambient pressure environment, where colliding droplets have increasing tendency for bouncing off instead of coalescence or separation predicted by the widely used Estrade et al.'s and O'Rourke's models. The uncertainty of the kinetic energy dissipation rate f_E, a key parameter in the pressure-dependent droplet collision model, was not found to cause qualitatively different predictions. By comparing the spray combustion characteristics between the cross- and opposed-impingement with and without swirl in the model OPCI, we found that the presence of strong swirling flow deflects sprays from impingement and therefore the opposed-impingement show better combustion performance by producing more spatially uniform droplet distribution, but spray cross-impingement enhances droplet collision hence promotes atomization in the absence of swirling flow.

Acknowledgements

The work was supported by the Hong Kong Research Grants Council/General Research Fund (PolyU 152217/14E and PolyU 152651/16E) in part by the National Natural Science Foundation of China (Grant No. 51406013).

References

[1] J.-P. Pirault, M. Flint, Opposed Piston Engines: Evolution, Use, and Future Applications, SAE international, 2010.

[2] P. Hofbauer, Opposed piston opposed cylinder (OPOC) engine for military ground vehicles, SAE Paper, 2005-01-1548 (2005).

[3] M. Franke, H. Huang, J.P. Liu, A. Geistert, P. Adomeit, Opposed Piston Opposed Cylinder (opoc™) 450 hp Engine: Performance Development by CAE Simulations and Testing, SAE Paper, 2006-01-0277 (2006).

[4] M. Flint, J. Pirault, Opposed piston engines: evolution, use, and future applications, SAE International, Warrendale, PA ISBN, (2009) 978-970.

[5] R.E. Herold, M.H. Wahl, G. Regner, J.U. Lemke, D.E. Foster, Thermodynamic benefits of opposed-piston two-stroke engines, SAE Paper, 2011-01-2216 (2011).

[6] S. Xu, Y. Wang, T. Zhu, T. Xu, C. Tao, Numerical analysis of two-stroke free piston engine operating on HCCI combustion, Appl. Energy, 88 (2011) 3712-3725.

[7] L. Huang, An Opposed-Piston Free-Piston Linear Generator Development for HEV, SAE Paper, 2012-01-1021 (2012).

[8] S. Naik, D. Johnson, J. Koszewnik, L. Fromm, F. Redon, G. Regner, K. Fuqua, Practical Applications of Opposed-Piston Engine Technology to Reduce Fuel Consumption and Emissions, SAE Paper, 2013-01-2754 (2013).

[9] G. Regner, D. Johnson, J. Koszewnik, E. Dion, F. Redon, L. Fromm, Modernizing the Opposed Piston, Two Stroke Engine for Clean, Efficient Transportation, SAE Paper, 2013-26-0114 (2013).

[10] R. Venugopal, N. Abani, R. MacKenzie, Effects of Injection Pattern Design on Piston Thermal Management in an Opposed-Piston Two-Stroke Engine, SAE Paper, 2013-01-2423 (2013).

[11] Z. Zhao, D. Wu, F. Zhang, Z. Zhang, Design and Performance Simulation of Opposed-Piston Folded-Cranktrain Engines, SAE Paper, 2014-01-1638 (2014).

[12] M. Huo, Y. Huang, P. Hofbauer, Piston Design Impact on the Scavenging and Combustion in an Opposed-Piston, Opposed-Cylinder (OPOC) Two-Stroke Engine, SAE Paper, 2015-01-1269 (2015).

[13] C.K. Law, Combustion physics, Cambridge university press, 2010.

[14] P. Brazier-Smith, S. Jennings, J. Latham, The interaction of falling water drops: coalescence, Proc. R. Soc. London, Ser.A, 326 (1972) 393-408.

[15] P.J. O'Rourke, Collective drop effects on vaporizing liquid sprays, in, Los Alamos National Lab., NM (USA), 1981.

[16] A.A. Amsden, P. O'rourke, T. Butler, KIVA-II: A computer program for chemically reactive flows with sprays, in, Los Alamos National Lab., NM (USA), 1989.

[17] Y. Jiang, A. Umemura, C. Law, An experimental investigation on the collision behaviour of hydrocarbon droplets, J. Fluid. Mech., 234 (1992) 171-190.

[18] J. Qian, C. Law, Regimes of coalescence and separation in droplet collision, J. Fluid. Mech., 331 (1997) 59-80.

[19] A. Munnannur, Droplet Collision Modeling in Multi-dimensional Engine Spray Computation, University of

Wisconsin Madison, 2007.

[20] A. Munnannur, R.D. Reitz, A new predictive model for fragmenting and non-fragmenting binary droplet collisions, Int. J. Multiphase Flow, 33 (2007) 873-896.

[21] S. Kim, D.J. Lee, C.S. Lee, Modeling of binary droplet collisions for application to inter-impingement sprays, Int. J. Multiphase Flow, 35 (2009) 533-549.

[22] Z. Zhang, Y. Chi, L. Shang, P. Zhang, Z. Zhao, On the role of droplet bouncing in modeling impinging sprays under elevated pressures, Int. J. Mass Transfer, 102 (2016) 657-668.

[23] D.P. Schmidt, C. Rutland, A new droplet collision algorithm, J. Comput. Phys., 164 (2000) 62-80.

[24] P. Nordin, Complex chemistry modeling of diesel spray combustion, Chalmers University of Technology, 2001.

[25] P.J. Tennison, T.L. Georjon, P.V. Farrell, R.D. Reitz, An experimental and numerical study of sprays from a common rail injection system for use in an HSDI diesel engine, SAE Paper, 980810 (1998).

[26] T.L. Georjon, R.D. Reitz, A drop-shattering collision model for multidimensional spray computations, Atomization Sprays, 9 (1999).

[27] G. Brenn, D. Valkovska, K. Danov, The formation of satellite droplets by unstable binary drop collisions, Phys. Fluid, 13 (2001) 2463-2477.

[28] R. Aumann, M. McCracken, J. Abraham, An evaluation of a composite model for predicting drop-drop collision outcomes in multidimensional spray computations, SAE Paper, 2002-0148-7191 (2002).

[29] S.L. Post, J. Abraham, Modeling the outcome of drop–drop collisions in Diesel sprays, Int. J. Multiphase Flow, 28 (2002) 997-1019.

[30] L.E. Kollár, M. Farzaneh, A.R. Karev, Modeling droplet collision and coalescence in an icing wind tunnel and the influence of these processes on droplet size distribution, Int. J. Multiphase Flow, 31 (2005) 69-92.

[31] Z. Zhang, P. Zhang, Kinetic energy recovery and interface hysteresis of bouncing droplets after inelastic head-on collision, Phys. Fluid, 29 (2017) 103306.

[32] P. Zhang, C.K. Law, An analysis of head-on droplet collision with large deformation in gaseous medium, Phys. Fluid, 23 (2011) 042102.

[33] J.-P. Estrade, H. Carentz, G. Lavergne, Y. Biscos, Experimental investigation of dynamic binary collision of ethanol droplets–a model for droplet coalescence and bouncing, Int. J. Heat Fluid Flow, 20 (1999) 486-491.

[34] T. Chiba, M. Saito, K. Amagai, M. Arai, Inter-spray impingement of two diesel sprays, in: Proc. Int. Conf. Liq. Atomization Spray Systems, 2000, pp. 16-20.

[35] Z. Zhang, P. Zhang, Z. Zhao, Spray Impingement and Combustion in a Model Opposed-Piston Compression Ignition Engine, Combust. Sci. Technol., 189 (2017) 1943-1965.

[36] M. Arai, M. Saito, Atomization characteristics of jet-to-jet and spray-to-spray impingement systems, Atomization

Sprays, 9 (1999) 399-417.

[37] Y. Maruyama, M. Saito, Effect of Inter-Impingement Process on the Behavior of a Diesel Spray, in: Proc. Int. Conf. Liquid Atomization and Spray Systems (ICLASS), Vol. 2001, 2001, pp. 241-246.

[38] S.H. Lee, G.H. Ko, H.S. Ryou, A numerical study on the spray-to-spray impingement system, KSME international journal, 16 (2002) 235-245.

[39] R. Krieger, G.L. Borman, Computation of apparent heat release for internal combustion engines, Mechanical Engineering, 89 (1967) 59-70.

[40] A.A. Amsden, T.D. Butler, P.J. Orourke, The KIVA-2 computer program for transient multidimensional chemically reactive flows with sprays, in: International fuels and lubricants meeting and exposition, Toronto, Canada, 2 Nov 1987, 1987.

[41] P.J. Orourke, A.A. Amsden, The TAB method for numerical calculation of spray droplet breakup, in: The International Fuels and Lubricants Meeting and Exposition, Toronto, Ontario, 2 Nov, 1987.

[42] Spalding, B. D., Lectures in mathematical models of turbulence, Academic Press, 1972.

[43] M. Orme, Experiments on droplet collisions, bounce, coalescence and disruption, Prog. Energy combust. Sci., 23 (1997) 65-79.

[44] D. Zhang, P. Zhang, Y. Yuan, T. Zhang, Hypergolic ignition by head-on collision of N, N, N′, N′－tetramethylethylenediamine and white fuming nitric acid droplets, Combust. Flame, 173 (2016) 276-287.

[45] J.B. Heywood, Internal combustion engine fundamentals, Mcgraw-hill New York, 1988.

Cross-Impingement and Combustion of Sprays in High-Pressure Chamber and Opposed-piston Compression Ignition Engine

Zhenyu Zhang[a], Peng Zhang[a*]

[a] *Department of Mechanical Engineering, The Hong Kong Polytechnic University, Hong Kong, PR. China*

Abstract: Spray cross-impingement in a high-pressure chamber (10-30 atm) was studied experimentally, the results being compared to the spray opposed-impingement. The comparison was subsequently extended to the spray combustion in a model opposed-piston compression ignition engine. To account for the ambient pressure effects in collision outcomes, a recently proposed pressure-dependent droplet collision model was implemented in the KIVA-3V computer program for simulating the experiments. Compared with the widely used Estrade et al.'s and O'Rourke's models, the pressure-dependent model produces satisfactory predictions to spray characteristics. The uncertainty of the kinetic energy recovery coefficient, which affects the post-collision characteristics of bouncing droplets, was found to cause insignificant difference in model predictions. In the high-pressure chamber, droplet collisions in cross-impingement occur earlier than those in the opposed-impingement and result in more coalescence, consequently producing larger droplet sizes. With increasing the ambient pressure, the increasing tendency of droplet bouncing diminishes the difference of these two spray impingements. In the model OPCI, the presence of strong swirling flow deflects sprays from impingement and therefore the opposed-impingement shows slightly better combustion performance by producing more spatially uniform droplet distribution. However, the spray cross-impingement enhances droplet collision hence promotes atomization in the absence of swirling flow.

* Corresponding author
E-mail pengzhang.zhang@polyu.edu.hk.
Fax: (852)23654703 Tel: (852)27666664

Keywords: Spray impingement; Droplet bouncing; Kinetic energy recovery coefficient; High-pressure chamber; Opposed-piston compression ignition.

1. Introduction

In recent years, there are rekindled interests in opposed-piston compression ignition (referred to as OPCI hereinafter) engines [1-12], where cylinder head is absent and fuel injectors are mounted on the cylinder liner. In order to sufficiently utilize the in-cylinder air, two fuel injectors are usually so oriented that their sprays tend to impinge with each other, rendering binary droplet collision a frequent event in cylinder. It is evident that the collision outcomes, such as droplet bouncing, coalescence and separation, can substantially influence the size and velocity distributions of droplets and in turn the subsequent combustion and emission [13].

Earlier experiment [14] on water droplet collision under atmospheric environment shows that the collision outcomes are either coalescence or stretching separation, depending on the collision Weber number, $We = 2\rho_l U^2 R_s/\sigma$, the impact parameter, $B = X/(R_s + R_L)$, and the size ratio $\Delta = R_s/R_L$, where ρ_l is the liquid density, U is the relative velocity of the colliding droplets, σ is the surface tension coefficient, X is the projection of the distance between the mass centers of the droplets in the direction normal to the relative velocity, R_s and R_L are the radii of smaller and larger droplets, respectively. This result was subsequently adopted by O'Rourke [15] in developing his droplet collision model, which is implemented in the widely used KIVA [16] computer program for the Eulerian-Lagrangian simulation of spray combustion.

By recognizing that liquid alkanes are more relevant to the hydrocarbon fuel, Jiang et al.'s [17] and Qian and Law's [18] experiments on droplet collision of liquid alkanes, for the first time, identify droplet bouncing as a commonly encountered collision outcome, which is however seldom seen for water droplet collision under atmospheric pressure and hence absent in O'Rourke's [15] collision model. Duo to its incomplete description on the main collision outcomes of hydrocarbon fuel droplet, the over-simplified O'Rourke's droplet collision model was subsequently improved by a number of models, which has been summarized in a few reviews [19-22]. Majority of the models aim to estimate the collision probability [23, 24], to reproduce the complex collision outcomes [19, 20, 22, 25-30], and to predict the post-collision characteristics of droplets [31]. However, the influence

of ambient pressure on droplet collision has never been concerned.

Although Qian and Law [18] experimentally confirmed that droplet bouncing is promoted by increasing ambient pressure and that the underlying physics has been theoretically delineated by Zhang and Law [32], no modelling effort was made previously to account for the influence of ambient pressure until very recently Zhang et al. [22] proposed a practically simple pressure-dependent droplet collision model based on the experiment results of Qian and Law [18] and the theoretical analysis of Zhang and Law [32]. Compared with the previous models, for example Estrade et al.'s [33] bouncing-coalescence model, which does not account for the fact that increasing of ambient pressure promotes droplet bouncing, the pressure-dependent model produces better predictions to the available experimental data [34] on impinging spray characteristic, especially under high ambient pressures.

Zhang et al. [35] also applied the pressure-dependent model to study spray impingement and combustion in a model OPCI engine, where two oppositely-oriented multiple-nozzle injectors with C_2 symmetry were investigated and optimized. Although the model again shows better performance than others in predicting the spray characteristics under high pressures, its advantage is not easily perceived when the in-cylinder swirling flow is sufficiently strong to deflect the inter-injector sprays (from two different injectors) from being impinged. The impingement of intra-injector spray (from two different nozzles of the same injector) is always presented and enhanced by the swirling flow, but it is not the same effective as the inter-injector spray impingement in promoting droplet collisions.

The present study was motivated by exploring new spray setup to promote inter-injector spray impingement, which has been found to enhance fuel atomization and subsequent fuel/air mixture and combustion [34, 36-38]. Recognizing that the in-cylinder swirl suppresses the inter-injector spray impingement from two opposed-oriented injectors, we audaciously proposed a spray setup with perpendicularly oriented injectors, which may result in the spray cross-impingement. The present study aims to experimentally and numerically investigate spray cross-impingement in a high-

pressure chamber and in a model OPCI engine, the results were compared with that of opposed-impingement. In the following text, we shall describe the experimental and numerical specifications of the cross-impingement sprays, in Section 2. The results and discussion of spray cross- and opposed-impingement in high-pressure chamber, in Section 3, followed by the spray combustion of cross- and opposed-impingement in a model OPCI, in Section 4.

2. Experimental Specifications and Numerical Methods

2.1 Spray layout of cross- and opposed-impingement

Figure 1 shows the schematic of spray cross- and opposed-impingement layouts. It should be noted that, the present cross-impingement spray layout was developed based on Zhao et al.'s [11] spray patterns, while the opposed-impingement layout was developed according to Hofbauer's [2] optimized results. The cross-impingement was developed to promote spray impingement and atomization, while opposed-impingement was designed to generate more uniform droplet distribution in the combustion chamber.

For the cross-impingement shown in Figure 1(a), each injector consists of three nozzles, No. 1 – No. 3 refers to one injector while No. 4 – No. 6 refers to the other one. No. 2 and No. 5 are on the Z=0 plane, No. 2 and No. 5, projections of No. 1 and No. 4 (similarly, No. 3 and No. 6) on Z=0 plane are symmetrical with respect to the plane X=Y. No. 1 and No. 3 (similarly, No. 4 and No. 6) are on the same plane with an angle of 3° respect to X=0 plane. The angles between No. 1 – No. 3 and the Y-axis on Z=0 plane are 45°, 5° and 30°, respectively. Similarly, angles between No. 4 – No. 6 and the X-axis on Z=0 plane are also 45°, 5° and 30°, respectively.

For the opposed-impingement shown in Figure 1(b), No. 1 – No. 3 are the same to that in cross-impingement, the opposed-impingement possesses the C_2 symmetry so that that No. 1 and No. 4 sprays (similarly, No. 2 and No. 5, and No. 3 and No. 6) can interchange their positions by rotating for 180° with respect to the Z=0 axis.

2.2 Experimental Apparatus

The experiment in the present paper contains two synergetic parts, which serve to validate the simulation for the non-reacting and isothermal sprays in constant-volume chamber and then for the reacting and variable-temperature sprays in an OPCI model engine.

The simplest the first, we investigated the non-reacting impinging sprays in a constant-volume chamber without heating; the temperature in the chamber was constant at 298K. The objective of the non-reacting impinging spray in the constant volume vessel is to validate the adopted pressure-dependent droplet collision model. Isothermal chamber suppresses droplet evaporation so that liquid droplets in the chamber have longer residence time, which facilitates the comparison of the predictions from different droplet collision models (i.e., O'Rourke's [16] model, Estrade et al.'s [33] model and the pressure-dependent model [22]). It is extremely difficult to experimentally measure the spray evolution in the operating engine, although it definitely merits future study. Subsequently, we extended the investigation to the combustion of cross-impingement impinging sprays in an opposed-piston compression ignition (OPCI) engine, where the moving pistons make the chamber flow statistically unsteady. The combustion temperature, varying with the crank angle, is similar to that in real engines.

Schematics of the experimental apparatus for non-reacting cross- and opposed-impingement sprays in a high-pressure chamber and cross-impinging spray combustion in a model OPCI engine are shown in Figure 2(a) and 2(b). A complete description of the experimental apparatus for impinging sprays can be found in our previous publication [22], so only a brief description of the experimental set up will be given here. For non-reacting spray impingement, time-resolved shadowgraph images in the chamber (1) with two opposed glass windows were taken by a Fastcam SA4 camera (10000 fps) (2) combined with a stroboscope (3). The chamber was filled with pure nitrogen with varying pressure at 10 atm, 20 atm, and 30 atm, respectively. A Bosch CP1H3 common rail system (4) was adopted for fuel injection. The injection pressure was 160 MPa and the injection duration was 1.5 ms with total of 90 mg/cycle liquid diesel was injected into the chamber

by two injectors, simultaneously.

The model OPCI (5) with 100 mm in bore and 110 mm in stroke for each piston is schematized in Figure 2(b). Similarly, the detailed description of OPCI working principle can be found in one of our previous publication [35]. For a briefly introduce, the engine prototype has two cylinders and a total displacement of 3.4 liters with the rated speed is 2100 rpm. Each cylinder contains two oppositely moving pistons, namely, intake piston and exhaust piston, respectively. Thus, cylinder head is absent and fuel injectors can only be installed on the cylinder liner. The OPCI engine employs a port-to-port uniflow scavenging system for gas exchange, and the port opening and closing are controlled by corresponding pistons. In this study, the exhaust ports open at 100° ATDC (after top dead center) and close at 113° BTDC (before top dead center); the intake ports open at 116° ATDC and close at 110° BTDC. Engine power and torque were measured by an electrical dynamometer. A Kistler-6056A cylinder pressure transducer (6) together with a Kistler 2614B crank angle sensor (7) were used to collect the cylinder pressure data with a crank angle interval of 0.2° CA and for 200 engine cycles. The pressure data was used to estimate heat release rate by using Krieger and Borman's [39] method. Intake pressure and exhaust pressure were measured by a Kistler 4005B pressure sensor (8) and a Kistler 4049A pressure senor (9), respectively. The measured intake and exhaust pressure were adopted to set up the numerical simulation, while the measured cylinder pressure was used to estimate heat release rate and validate the simulation results.

2.3 Numerical Methodology

Reynolds Average Navier-Stokes (RANS) calculations were adopted in the present study by using the widely used computer program KIVA-3V. The standard k-ε model [40] was adopted for turbulence modelling and the SIMPLEC method [15] for velocity-pressure coupling. The TAB model [41] and Spalding model [42] were used to account for the subsequent droplet breakup and evaporation, respectively. The Arrhenius law [16] was used to calculate chemical reaction rate constants. The pressure-dependent droplet collision model, which accounts for the propensity of droplet bouncing with increasing ambient pressure and proposed by Zhang et al. [22], was adopted to

account for droplet collision. Simultaneously, the widely used O'Rourke's [15] and Estrade et al.'s [33] droplet collision model were also used to calculate non-reaction spray characteristic for a comparison.

Figure 3 illustrates the *We-B* regime nomogram (for n-hexadecane droplets) for Zhang et al.'s [22], Estrade et al.'s [33] and O'Rourke's [15] model, respectively. For Zhang et al.'s model shown in Figure 3(a), to account for that bouncing is promoted by increasing the ambient pressure, Estrade et al.'s bouncing criterion was modified by adding a pressure-dependent factor $g(p)$ determined by fitting Qian and Law's [18] experimental data, given by

$$We < We_{cr}(p,\Delta,B) = g(p)\cdot We_{cr}(1,1,0)\frac{\Delta(1+\Delta^2)(4\Theta'-12)}{2.8\chi_1\{\cos[\sin^{-1}(B)]\}^2} \quad (1)$$

with $g(p) = 0.25p + 0.75$. Here, $We_{cr}(p,\Delta,B)$ is the bouncing-coalescence transition Weber number at various p, Δ, and B. $We_{cr}(1,1,0) = 15.5$ for n-hexadecane was adopted in the present study [43]. The Estrade et al.'s model shown in Figure 3(b) was developed according to the experimental observation on ethanol droplet collision [33] under atmospheric pressure, only bouncing and coalescence are considered in this model, and the bouncing criterion can be written as

$$We < \frac{\Delta(1+\Delta^2)(4\Theta'-12)}{\chi_1\{\cos[\sin^{-1}(B)]\}^2} \quad (2)$$

the RHS of Eq.(2) is equal to 2.8 for $\Delta = 1.0$ and $B = 0$, corresponding to the constant term in the denominator of Eq.(1). In Eq.(1) and (2), the shape factor $\Theta' = 3.351$ and χ_1 is determined by $\chi_1 = 1 - 0.25(1+\tau)(2-\tau)^2$ if $(r_1 + r_2)(1 - B) > r_1$, otherwise, $\chi_1 = 0.25(3-\tau)\tau^2$, where $\tau = (1 - B)(1 + \Delta)$.

Unlike Estrade et al.'s [33] and Qian and Law's [18] experiment on hydrocarbon droplets, O'Rourke's [15] model was developed by Brazier-Smith et al.'s [14] experimental observation on water droplet collision, hence droplet bouncing is absent but involving in stretching separation without fragmentation (a.k.a. grazing), as shown in Figure 3(c). The stretching separation criterion

can be written as

$$B > B_{cr} = \sqrt{\min\{1.0,\ 2.4(\Delta^{-3} - 2.4\Delta^{-2} + 2.7\Delta^{-1})/We\}} \tag{3}$$

Furthermore, it is noted that the narrow bouncing regime in Estrade et al.'s model tends to predict more droplet coalescence and therefore larger droplet size than the other two models.

Because the boundary between bouncing and coalescence right shifts to higher Weber number with ambient pressure increasing, droplet bouncing is considered as the primary collision outcome for prevalent droplet size and velocity [18]. Recognizing that droplet bouncing or grazing are inelastic, the post-collision velocity can be determined by

$$u_{n,i} = \frac{u_i R_i^3 + u_j R_j^3 + R_j^3 (u_i - u_j)\sqrt{1 - f_E}}{R_i^3 + R_j^3} \tag{4}$$

here, u is the droplet velocity, the subscript n denotes the droplet after bouncing, i and j refer to two interacting droplets, f_E is the kinetic energy dissipation factor and $1 - f_E$ can be regard as the kinetic energy recovery coefficient, which shall be discussed in Section 3.3.

A cubic computational domain of (100 mm)^3 and a uniform Cartesian mesh with 125,000 grid cells of (2 mm)^3 were used to simulate spray cross-impingement and opposed-impingement in the high-pressure chamber, as shown in Figure 4(a). It should be noted that, the mesh independence study has been done in our previous publications [22]. For a briefly summary, the evolution of the predicted spray penetration length with time of Chiba et al.'s [34] experiment for six different meshes from the coarsest $5 \times 5 \times 5$ mm^3 to the finest $1 \times 1 \times 1$ mm^3. The calculated results show a significant dependence on the cell size coarser than $2 \times 2 \times 2$ mm^3, beyond which the grid-dependence is substantially reduced. Similar cell size also adopted by Kim et al. [21] for their impinging spray simulation. Boundary effects in this calculation can be neglected in the present problem because the domain size is much larger than the size of the sprays and the penetration length. Consequently, the domain boundaries can be simply set as isothermal walls of 298 K and with the nonslip conditions for velocity.

In order to investigated spray combustion characteristic in the OPCI with varying volume and ambient pressure. Spray combustion of cross- and opposed-impingement in the OPCI engine was simulated by using a full-scale three-dimensional dynamic mesh with intake ports and exhaust ports, containing 200615 cells at BDC (bottom dead center) and 32748 cells at TDC (top dead center) after rezone, as shown in Figure 4(b). Intake port was cut into an angle of 20° so as to generate in-cylinder swirl. Liquid diesel was injected into the combustion chamber in the form of droplet parcels. In the Eulerian-Lagrangian simulation, each parcel usually represents many droplets. In this study we assumed the parcel number density is 1000 parcels/mg for both non-reaction spray calculation and spray combustion simulation in the OPCI engine. The full cycle calculation starts at 100° ATDC and ends at 80° BTDC. Initial and boundary conditions, such as intake pressure and temperature, exhaust pressure and temperature, were set according to the experimental data, to be elucidated in the following text. The mesh independence studies on the adopted dynamic mesh also can be found in one of our previous publication [35], and will not repeat in this paper.

Spray layouts for cross- and opposed-impingement were set up according to the experimental conditions, which has been discussed in the Section 2.1. Non-reaction spray characteristics for cross- and opposed-impingement in the constant volume chamber were calculated and a typical run takes about half an hour on an Inter Xeon E5 2692 central processing unit (CPU), while a typical run of full engine cycle for cross- or opposed-impingement combustion takes around 48 CPU hours.

3. Spray cross-impingement in high-pressure chamber

3.1 Experimental and Numerical Shadowgraph Images

Figure 5 shows the impinging spray shadowgraphs at selected time instants under different ambient pressures. The numerical shadowgraph was obtained by taking the second-order derivative of density in the domain. A complete set of experimental and simulation results of spray cross-impingement during the entire process can be found in Fig. S1-Fig. S3 in the Supplemental Material. Figure 5(a) shows the spray cross-impingement at 10 atm. From injection time (i.e., t =0 ms) to t =

0.5 ms when the spray impingement is about to occur, no significant difference between experimental and simulation shadowgraphs can be observed for all the droplet collision models. This is because droplets in the early stage are dominated by aerodynamic deceleration and breakup. In the later stage after t = 0.5 ms, droplet collision become more frequent, but only slight difference among the predictions of the three models can be seen. This is because the aerodynamic deceleration in the gas chamber of 10 atm is insufficiently strong so that the collision *We*s are mostly large enough to affect droplet coalescence. It is evident from Figure 3 that all the models show no significant difference in predicting droplet coalescence at sufficiently large *We* and small *B*.

Figure 5(b) shows the spray cross-impingement at 20 atm. For the same reason stated above, only slight difference among three model predictions can be observed before spray impingement is about to occur by t =1.0 ms. After spray impingement starts, Zhang et al.'s model predicts more droplet parcels than other two models do, because it predicts higher transition *We* for droplet coalescence at increased pressure and therefore more bouncing droplets with unchanged droplet size and reduced inertia (due to inelastic collisions to be discussed in Section 3.3). It is also seen that Estrade et al.'s and O'Rourke's model predict multi-tips spray shape, probably due to the over-predicted droplet sizes and inertia and hence larger shadow regions, but this prediction is not verified by either experimental shadowgraphs or the prediction of Zhang et al.'s model.

Figure 5(c) shows the spray cross-impingement at 30 atm. For comparison, the spray opposed-impingement at 30 atm is also shown in Figure 5(d). It should be noted that, spray opposed-impingement results has been studied in one our previous publication [22]. Owing to its correctly accounting for the pressure-dependence of droplet collision, Zhang et al.'s model predicts results more similar to the experimental images in both cases. Spray impingement (between No. 3 and No. 6 sprays) occurs earlier in Figure 5(c) at around t =1.0 ms, when the spray impingement in Figure 5(d) has not yet happened. It is also seen that the spray opposed-impingement seems to produce more spatially uniform distribution of droplets, which spread out in the chamber center. These spray characteristics may influence combustion characteristics in the OPCI engine, to be discussed in

Section 4.

3.2 Quantitative Comparison of Experiment and Simulation

A grayscale level analysis [22, 44] of shadowgraph images was adopted in the present study for quantitative comparison of different droplet collision models. The time-dependent ratio $r_d = N_d(t \mid G < G_{low})/N_t$ was defined as an indicator of spray spread based on the physical understanding that, in the gray-scale shadowgraph images of impinging spray, the dark areas represent either the droplets or the opaque gaseous species and have the grayscale levels (G=0 for the darkest and G=256 for the brightest) below a threshold value G_{low}. Consequently, $N_d(t \mid G < G_{low})$ is the pixels number in the image with the grayscale level less than G_{low} at the time instant t, and N_t is the total pixels number in the shadowgraph image at the same time instant. Figure 6 shows the evolution of r_d calculated from the experimental and numerical shadowgraphs for different G_{low}. Although all the predictions show good agreement with the experimental results for spray impingement before fuel injection ends, the predicted r_d slightly differ between the models, and Zhang et al.'s model produces increasingly better predictions with increasing pressure. However, moderate discrepancies can be found for the long-time behaviors of droplets after fuel injection ends, and may be attributed to the computational and model uncertainties associated with droplet breakup and vaporization, which become increasingly dominant processes with time. It is also observed that, numerical simulation slightly over-predicts r_d, probably due to the uncertainty of kinetic energy recovery coefficient f_E, to be discussed in the following section.

For further quantitative comparison, the predicted Sauter mean diameters (SMD) which were calculated by averaging the entire droplet diameter in the calculation domain are shown in Figure 7. Note that the experimental data is absent in this comparison because it is difficult to measure the overall SMD in the experiment by counting all the droplet sizes in the chamber. As anticipated, Zhang et al.'s model predicts smaller SMD than others, and the the difference among different model predictions increases with the ambient pressure. This is because Zhang et al.'s model predicts increasingly larger transition We for droplet coalescence with increasing ambient pressure and

consequently more droplet bouncing. The propensity of droplet bouncing at increased ambient pressure is further enhanced by the increased aerodynamic deceleration of droplets, which effect more collisions with smaller *We*s. These results on SMD can be used to explain the discrepancies in r_d among different droplet collision models: Estrade et al.'s and O'Rouke's models tend to over-predict the likelihood of droplet coalescence and hence result in larger droplet size and spreading.

Figure 7 also compares the spray cross-impingement and opposed-impingement for the SMDs predicted by Zhang et al.'s model. It is seen that the spray opposed-impingement has significantly smaller SMD at 10 atm than cross-impingement does, but the discrepancy declines at 20 atm and almost disappears at 30 atm. This can be understood by noting that the cross-impingement occurs earlier and results in more collisions with large *We*s to effect coalescence. With increasing the pressure, the increasing tendency of droplet bouncing diminishes the difference of these two spray impingements.

3.3 Influence and Uncertainty of Kinetic Energy Recovery Coefficient

The kinetic energy recovery coefficient is a key parameter in modelling post-collision characteristics of bouncing droplets, and is defined by O'Rourke [15] as $1 - f_E$, where f_E is the kinetic dissipation rate after bouncing. The determination of f_E entails either experimentally measuring the velocity changes during each collision or computationally tracking droplet interface and internal flow, both of which are beyond the scope of the present study. Recently, Zhang and Zhang [31] numerically simulated the kinetic energy recovery of bouncing droplets after inelastic head-on collision. However, employing their results in the present simulation is premature because the influence of ambient pressure and impact parameter remains unsolved.

To investigate the influence of the uncertainty of f_E on the present simulation, f_E was varied from elastic collision ($f_E = 0$) to totally inelastic collision ($f_E = 1.0$). Figure 8 shows the predictions of r_d and SMD for different f_E. It is seen that r_d and SMD decreases with increasing f_E. This can be understood by recognizing that a larger f_E means a smaller post-collision droplet velocity,

which results in a lower *We* for the subsequent collision and in turn increase the trend of droplet bouncing without size growth. Correlation between f_E with various collision parameters merits future studies on the fundamental phenomena of binary droplet collisions.

4. Spray Cross-impingement and Combustion in OPCI

It is seen above that the spray cross-impingement promotes droplet collision and spray atomization, and hence holds potential of enhancing combustion efficiency. Nevertheless, the spray cross-impingement setup also results in the spatially asymmetric droplet distribution in the combustion chamber and therefore may reduce combustion efficiency [2, 3]. Thus, we compared the spray combustion characteristics between cross- and opposed-impingement with and without swirl in the model OPCI, as shown in Figure 9. Figure 9(a)-(c) show the simulation results at engine speed of 2100 rpm and under 50% load. The simulation results of cross-impingement are validated by the experimental results for cylinder pressure and estimated heat release rate. Figure 9(d)-(f) extend the comparison to the same engine speed but under 100% load; Figure 9(g)-(i) to the same operating condition but without in-cylinder swirl. It should be noted that, in-cylinder swirl was generated by cutting intake port into an angle of 20°. For non-swirl case, this angle was set as 0° in the dynamic mesh. Intake temperature was set as 325 K; intake pressure was 1.2 bar and 1.6 bar for 50% and 100% load, respectively. Full engine cycle was calculated for each case, the calculation starts at 100° ATDC and ends at 80° BTDC.

4.1 Cylinder pressure and estimated heat release rate

Figures 9 (a), (d) and (g) show the in-cylinder pressure (*p*, left Y-axis) and the heat release rate (HR, right Y-axis) at different loads. Experiment cylinder pressure and the estimated heat release rate of cross-impingement spray combustion for 50% load are shown in Figure 9(a) to validate the numerical platform. SOI and EOI denote the start and end of injection. Fuel injection starts at -5° ATDC and ends at 12° ATDC for 50% load, and starts at -8° ATDC and ends at 13° ATDC for 100% loads. Good agreement between experiment and simulation for cylinder pressure *p* can be seen

in Figure 9(a), and the peak value of calculated heat release rate is slightly higher than estimated heat release by using Krieger and Borman's [39] approximation method, probably due to the experimental errors in pressure measurement and the computational uncertainties associated with simplified models for fuel vaporization and combustion. It is also interesting to observe that opposed-impingement produces a higher peak heat release rate and p than cross-impingement does either for the cases with 50% load and 100% load and with swirling flow. However, cross-impingement predicts moderately higher peak heat release rate and p for the case without swirling flow. These results accord with previous findings [35] and our hypothesis stated above that the presence of strong swirling flow deflects sprays from impingement and therefore the opposed-impingement spray setup shows better combustion performance by producing more spatially uniform droplets, as shown in Figure 10(a). In the absence of swirling flow, the influence of spray impingement in enhancing droplet collisions is more prominent for the cross-impingement spray setup, shown in Figure 10(b). More detailed explanations are as follows.

4.2 Evaporation and fuel/air mixture

To explain the above observations, we calculated a time-dependent ratio, $A_{\mathrm{d}} = N_{\mathrm{p}}(t)\mathrm{SMD}^2(t)/N_{\mathrm{p}}(0)\mathrm{SMD}^2(0)$, where $N_{\mathrm{p}}(0)$ and $\mathrm{SMD}(0)$ are the initial parcel number and SMD of droplets, as an indicator of total droplet surface area. Figures 9(b), (e) and (h) show the evolutions of A_{d} (left Y-axis) and premixed fuel mass (m_p, right Y-axis). For 50% load with in-cylinder swirl, no significant difference can be observed on A_{d} and hence on m_p, because fewer fuel droplets were injected into combustion chamber, leading to infrequent droplet collision. With the engine load is increased to 100%, opposed-impingement produces significant higher A_{d} around 2° ATDC and hence the higher premixed fuel mass. By contrast, the non-swirl case shows an opposite tend in that cross-impingement produces higher A_{d} and hence m_p, as shown in Figure 9(h). This also can be used to explain why cross-impingement predicts smaller peak value of heat release rate in the swirl cases but higher peak value in the non-swirl case.

4.3 Droplet size and number density

Figure 9(c), (f) and (i) show the evolutions of the droplet size (SMD, left Y-axis) and the parcel number (N_p, right Y-axis) for different loads. Following the previous study [35], we assumed the initial droplet number density is 1000 parcels/mg. For the same reason stated above, there is no significant difference between two spray setups for 50% load. Larger SMD and lower N_p after TDC can be seen at 100% load in the swirl case, implying that cross-impingement causes more collisions with higher Weber numbers and hence more coalescence, as shown in Figure 9(f). However, for the non-swirl case shown in Figure 9(i), due to the high collision frequency and kinetic energy dissipation, cross-impingement produces more droplet bouncing hence smaller SMD and higher N_p, as explained in the Section 3.3. To the end, although cross-impingement promotes spray atomization, the effects of in-cylinder swirl in impinging-spray combustion are significant by changing in-cylinder gas motion and fuel droplet distribution.

4.4 Engine-indicated thermal efficiency

To facilitate the comparison of spray combustion characteristic in the OPCI between cross- and opposed-impingement, Figure 11 compares the engine-indicated thermal efficiency η_i for different cases corresponding to the Figure 9. The efficiency η_i is defined by [45]

$$\eta_i = \frac{\oint pdV}{m_f Q_{LHV}} \tag{5}$$

where p is the predicted cylinder pressure, V is the engine displacement volume, m_f is the total fuel injection quantity per cycle, and Q_{LHV} is the low heating value of the fuel.

It is seen from Figure 11 that, the opposed-impingement produces significantly higher η_i than does the cross-impingement for both the case of 50% load and that of 100% load with swirling flow. However, the cross-impingement produces moderately higher η_i for the case without swirl. This again can be explained by that strong swirl flow deflects sprays from impingement and η_i is dominated by the uniform extent of droplet distribution. As discussed in Figure 5, the opposed-

impingement produces more uniform mixture hence higher η_i. However, the cross-impingement enhances spray atomization, which dominates η_i under the condition of non-swirl flow.

5. Concluding remarks

An experimental and numerical study was conducted on spray cross-impingement in the high-pressure chamber at 10-30 atm, and in the model OPCI engine, the results being compared to the spray opposed-impingement. The KIVA-3V simulation with the pressure-dependent droplet collision model [22] predicts satisfactorily the spray impingement and combustion in high ambient pressure environment, where colliding droplets have increasing tendency for bouncing off instead of coalescence or separation predicted by the widely used Estrade et al.'s and O'Rourke's models. The uncertainty of the kinetic energy dissipation rate f_E, a key parameter in the pressure-dependent droplet collision model, was not found to cause qualitatively different predictions. By comparing the spray combustion characteristics between the cross- and opposed-impingement with and without swirl in the model OPCI, we found that the presence of strong swirling flow deflects sprays from impingement and therefore the opposed-impingement show better combustion performance by producing more spatially uniform droplet distribution, but spray cross-impingement enhances droplet collision hence promotes atomization in the absence of swirling flow.

Acknowledgements

The work was supported by the Hong Kong Research Grants Council/General Research Fund (PolyU 152217/14E and PolyU 152651/16E) in part by the National Natural Science Foundation of China (Grant No. 51406013).

References

[1] J.-P. Pirault, M. Flint, Opposed Piston Engines: Evolution, Use, and Future Applications, SAE international, 2010.

[2] P. Hofbauer, Opposed piston opposed cylinder (OPOC) engine for military ground vehicles, SAE Paper, 2005-01-1548 (2005).

[3] M. Franke, H. Huang, J.P. Liu, A. Geistert, P. Adomeit, Opposed Piston Opposed Cylinder (opoc™) 450 hp Engine: Performance Development by CAE Simulations and Testing, SAE Paper, 2006-01-0277 (2006).

[4] M. Flint, J. Pirault, Opposed piston engines: evolution, use, and future applications, SAE International, Warrendale, PA ISBN, (2009) 978-970.

[5] R.E. Herold, M.H. Wahl, G. Regner, J.U. Lemke, D.E. Foster, Thermodynamic benefits of opposed-piston two-stroke engines, SAE Paper, 2011-01-2216 (2011).

[6] S. Xu, Y. Wang, T. Zhu, T. Xu, C. Tao, Numerical analysis of two-stroke free piston engine operating on HCCI combustion, Appl. Energy, 88 (2011) 3712-3725.

[7] L. Huang, An Opposed-Piston Free-Piston Linear Generator Development for HEV, SAE Paper, 2012-01-1021 (2012).

[8] S. Naik, D. Johnson, J. Koszewnik, L. Fromm, F. Redon, G. Regner, K. Fuqua, Practical Applications of Opposed-Piston Engine Technology to Reduce Fuel Consumption and Emissions, SAE Paper, 2013-01-2754 (2013).

[9] G. Regner, D. Johnson, J. Koszewnik, E. Dion, F. Redon, L. Fromm, Modernizing the Opposed Piston, Two Stroke Engine for Clean, Efficient Transportation, SAE Paper, 2013-26-0114 (2013).

[10] R. Venugopal, N. Abani, R. MacKenzie, Effects of Injection Pattern Design on Piston Thermal Management in an Opposed-Piston Two-Stroke Engine, SAE Paper, 2013-01-2423 (2013).

[11] Z. Zhao, D. Wu, F. Zhang, Z. Zhang, Design and Performance Simulation of Opposed-Piston Folded-Cranktrain Engines, SAE Paper, 2014-01-1638 (2014).

[12] M. Huo, Y. Huang, P. Hofbauer, Piston Design Impact on the Scavenging and Combustion in an Opposed-Piston, Opposed-Cylinder (OPOC) Two-Stroke Engine, SAE Paper, 2015-01-1269 (2015).

[13] C.K. Law, Combustion physics, Cambridge university press, 2010.

[14] P. Brazier-Smith, S. Jennings, J. Latham, The interaction of falling water drops: coalescence, Proc. R. Soc. London, Ser.A, 326 (1972) 393-408.

[15] P.J. O'Rourke, Collective drop effects on vaporizing liquid sprays, in, Los Alamos National Lab., NM (USA), 1981.

[16] A.A. Amsden, P. O'rourke, T. Butler, KIVA-II: A computer program for chemically reactive flows with sprays, in, Los Alamos National Lab., NM (USA), 1989.

[17] Y. Jiang, A. Umemura, C. Law, An experimental investigation on the collision behaviour of hydrocarbon droplets, J. Fluid. Mech., 234 (1992) 171-190.

[18] J. Qian, C. Law, Regimes of coalescence and separation in droplet collision, J. Fluid. Mech., 331 (1997) 59-80.

[19] A. Munnannur, Droplet Collision Modeling in Multi-dimensional Engine Spray Computation, University of

Wisconsin Madison, 2007.

[20] A. Munnannur, R.D. Reitz, A new predictive model for fragmenting and non-fragmenting binary droplet collisions, Int. J. Multiphase Flow, 33 (2007) 873-896.

[21] S. Kim, D.J. Lee, C.S. Lee, Modeling of binary droplet collisions for application to inter-impingement sprays, Int. J. Multiphase Flow, 35 (2009) 533-549.

[22] Z. Zhang, Y. Chi, L. Shang, P. Zhang, Z. Zhao, On the role of droplet bouncing in modeling impinging sprays under elevated pressures, Int. J. Mass Transfer, 102 (2016) 657-668.

[23] D.P. Schmidt, C. Rutland, A new droplet collision algorithm, J. Comput. Phys., 164 (2000) 62-80.

[24] P. Nordin, Complex chemistry modeling of diesel spray combustion, Chalmers University of Technology, 2001.

[25] P.J. Tennison, T.L. Georjon, P.V. Farrell, R.D. Reitz, An experimental and numerical study of sprays from a common rail injection system for use in an HSDI diesel engine, SAE Paper, 980810 (1998).

[26] T.L. Georjon, R.D. Reitz, A drop-shattering collision model for multidimensional spray computations, Atomization Sprays, 9 (1999).

[27] G. Brenn, D. Valkovska, K. Danov, The formation of satellite droplets by unstable binary drop collisions, Phys. Fluid, 13 (2001) 2463-2477.

[28] R. Aumann, M. McCracken, J. Abraham, An evaluation of a composite model for predicting drop-drop collision outcomes in multidimensional spray computations, SAE Paper, 2002-0148-7191 (2002).

[29] S.L. Post, J. Abraham, Modeling the outcome of drop–drop collisions in Diesel sprays, Int. J. Multiphase Flow, 28 (2002) 997-1019.

[30] L.E. Kollár, M. Farzaneh, A.R. Karev, Modeling droplet collision and coalescence in an icing wind tunnel and the influence of these processes on droplet size distribution, Int. J. Multiphase Flow, 31 (2005) 69-92.

[31] Z. Zhang, P. Zhang, Kinetic energy recovery and interface hysteresis of bouncing droplets after inelastic head-on collision, Phys. Fluid, 29 (2017) 103306.

[32] P. Zhang, C.K. Law, An analysis of head-on droplet collision with large deformation in gaseous medium, Phys. Fluid, 23 (2011) 042102.

[33] J.-P. Estrade, H. Carentz, G. Lavergne, Y. Biscos, Experimental investigation of dynamic binary collision of ethanol droplets–a model for droplet coalescence and bouncing, Int. J. Heat Fluid Flow, 20 (1999) 486-491.

[34] T. Chiba, M. Saito, K. Amagai, M. Arai, Inter-spray impingement of two diesel sprays, in: Proc. Int. Conf. Liq. Atomization Spray Systems, 2000, pp. 16-20.

[35] Z. Zhang, P. Zhang, Z. Zhao, Spray Impingement and Combustion in a Model Opposed-Piston Compression Ignition Engine, Combust. Sci. Technol., 189 (2017) 1943-1965.

[36] M. Arai, M. Saito, Atomization characteristics of jet-to-jet and spray-to-spray impingement systems, Atomization

Sprays, 9 (1999) 399-417.

[37] Y. Maruyama, M. Saito, Effect of Inter-Impingement Process on the Behavior of a Diesel Spray, in: Proc. Int. Conf. Liquid Atomization and Spray Systems (ICLASS), Vol. 2001, 2001, pp. 241-246.

[38] S.H. Lee, G.H. Ko, H.S. Ryou, A numerical study on the spray-to-spray impingement system, KSME international journal, 16 (2002) 235-245.

[39] R. Krieger, G.L. Borman, Computation of apparent heat release for internal combustion engines, Mechanical Engineering, 89 (1967) 59-70.

[40] A.A. Amsden, T.D. Butler, P.J. Orourke, The KIVA-2 computer program for transient multidimensional chemically reactive flows with sprays, in: International fuels and lubricants meeting and exposition, Toronto, Canada, 2 Nov 1987, 1987.

[41] P.J. Orourke, A.A. Amsden, The TAB method for numerical calculation of spray droplet breakup, in: The International Fuels and Lubricants Meeting and Exposition, Toronto, Ontario, 2 Nov, 1987.

[42] Spalding, B. D., Lectures in mathematical models of turbulence, Academic Press, 1972.

[43] M. Orme, Experiments on droplet collisions, bounce, coalescence and disruption, Prog. Energy combust. Sci., 23 (1997) 65-79.

[44] D. Zhang, P. Zhang, Y. Yuan, T. Zhang, Hypergolic ignition by head-on collision of N, N, N′, N′－tetramethylethylenediamine and white fuming nitric acid droplets, Combust. Flame, 173 (2016) 276-287.

[45] J.B. Heywood, Internal combustion engine fundamentals, Mcgraw-hill New York, 1988.

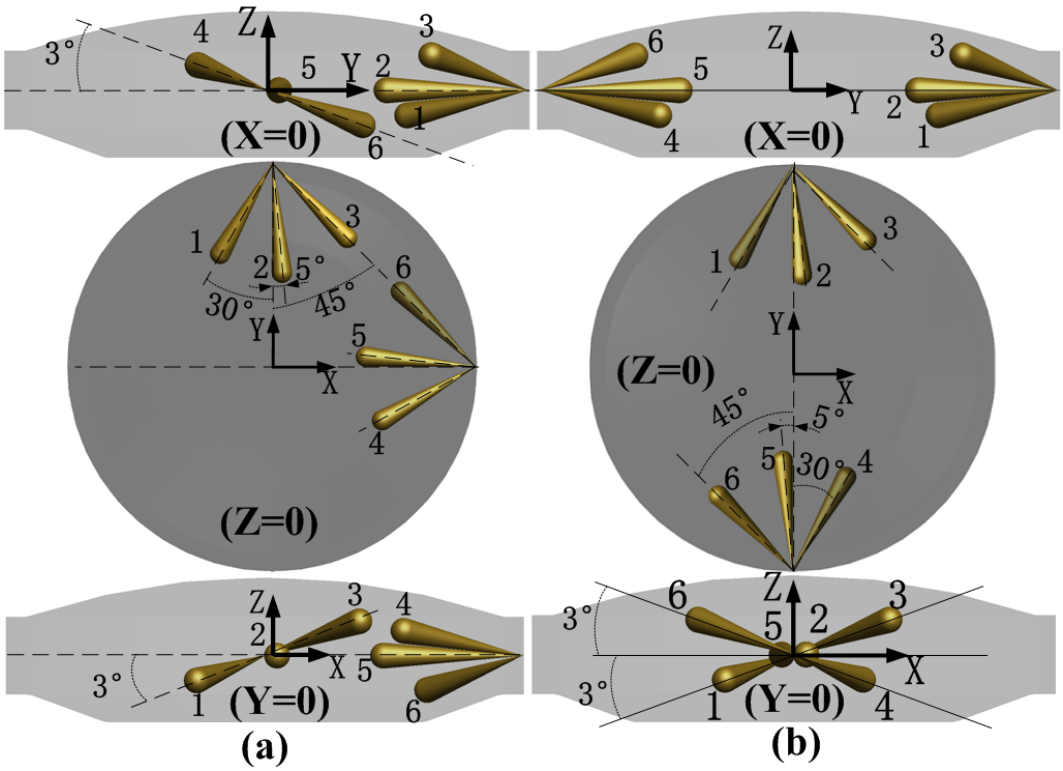

Figure 1. Schematic of fuel spray impingement layout: (a) cross-impingement and (b) opposed-impingement. The projections of each layout to the planes of X=0, Z=0 and Y=0 are from top to bottom. The shadows are the edge of combustion chamber.

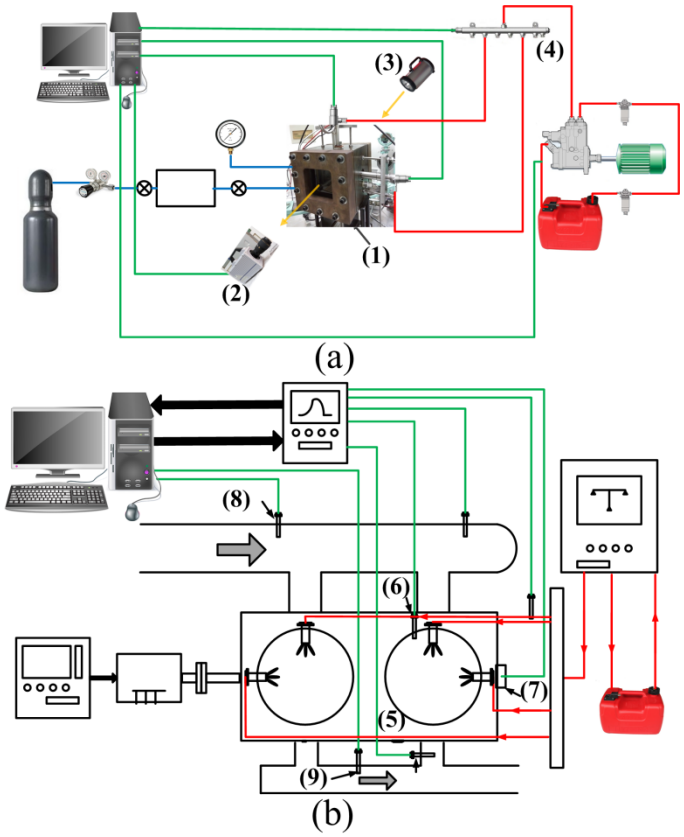

Figure 2. Schematic of experiment apparatus for spray cross-impingement in (a) a high-pressure chamber and (b) in a model OPCI engine. (1) constant-volume chamber, (2) camera, (3) stroboscope, (4) common rail system, (5) OPCI engine prototype, (6) cylinder pressure transducer, (7) crank angle sensor, (8) intake pressure sensor, (9) exhaust pressure sensor.

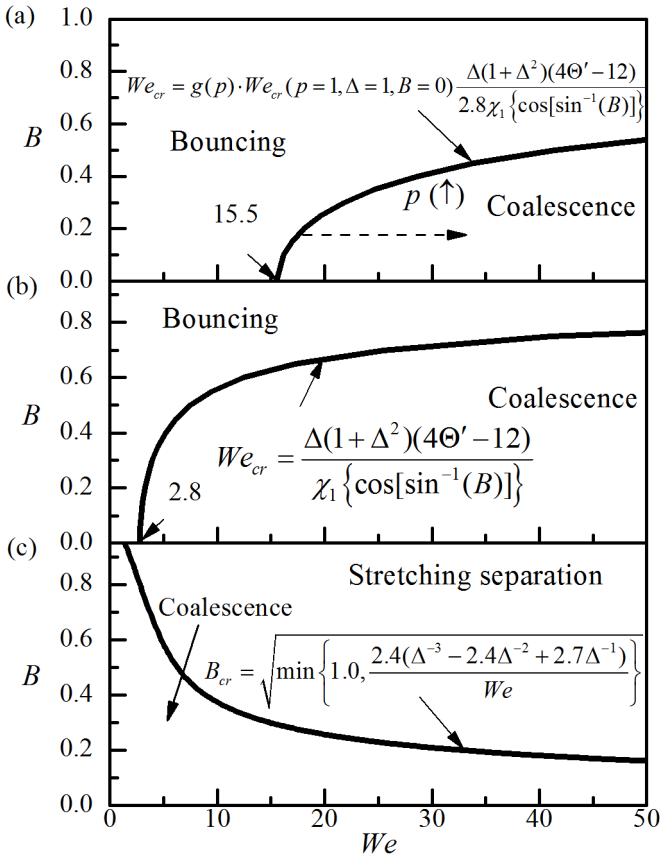

Figure 3. *We*-*B* (*Δ*=1.0) Regime nomograms of droplet collision underlie (a) Zhang et al.'s [22] pressure-dependent model, (b) Estrade et al.'s [33] model and (c) O'Rourke's [15] model.

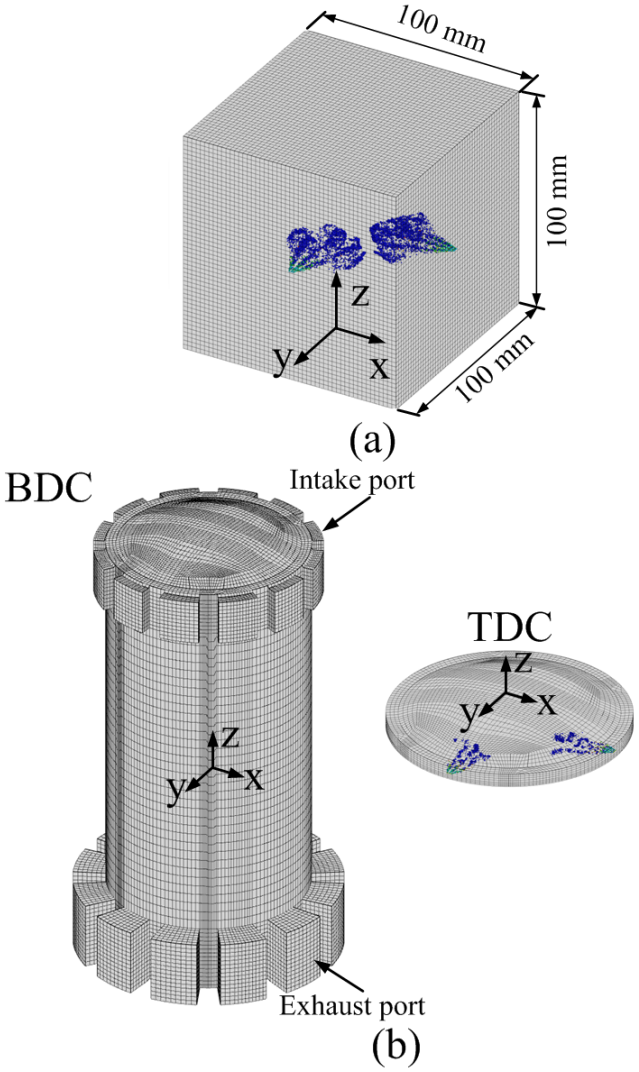

Figure 4. Three-dimensional cubic computational mesh for (a) cross- and opposed-impingement in the high-pressure chamber and (b) cross- and opposed-impingement spray combustion in the OPCI engine.

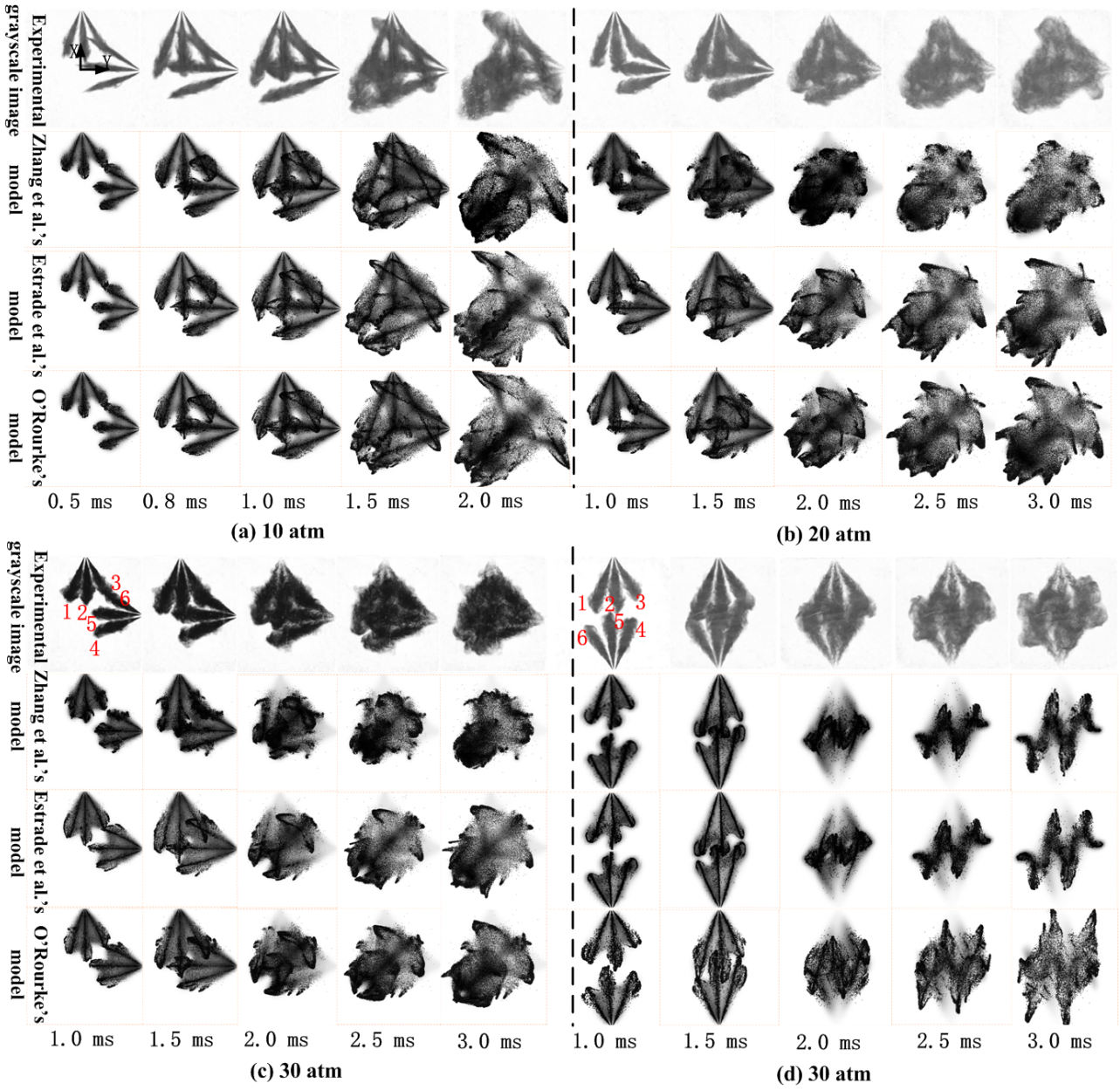

Figure 5. Experimental and numerical shadowgraphs of the spray cross-impingement at (a) 10 atm, (b) 20 atm, (c) 30 atm, and (d) the spray opposed-impingement at 30 atm (zhang et al., 2016b) [22]. Droplet parcels are shown in the numerical shadowgraphs. A complete set of experimental and simulation results of spray cross-impingement during the entire process can be found in Fig. S1-Fig. S3 in the Supplemental Material.

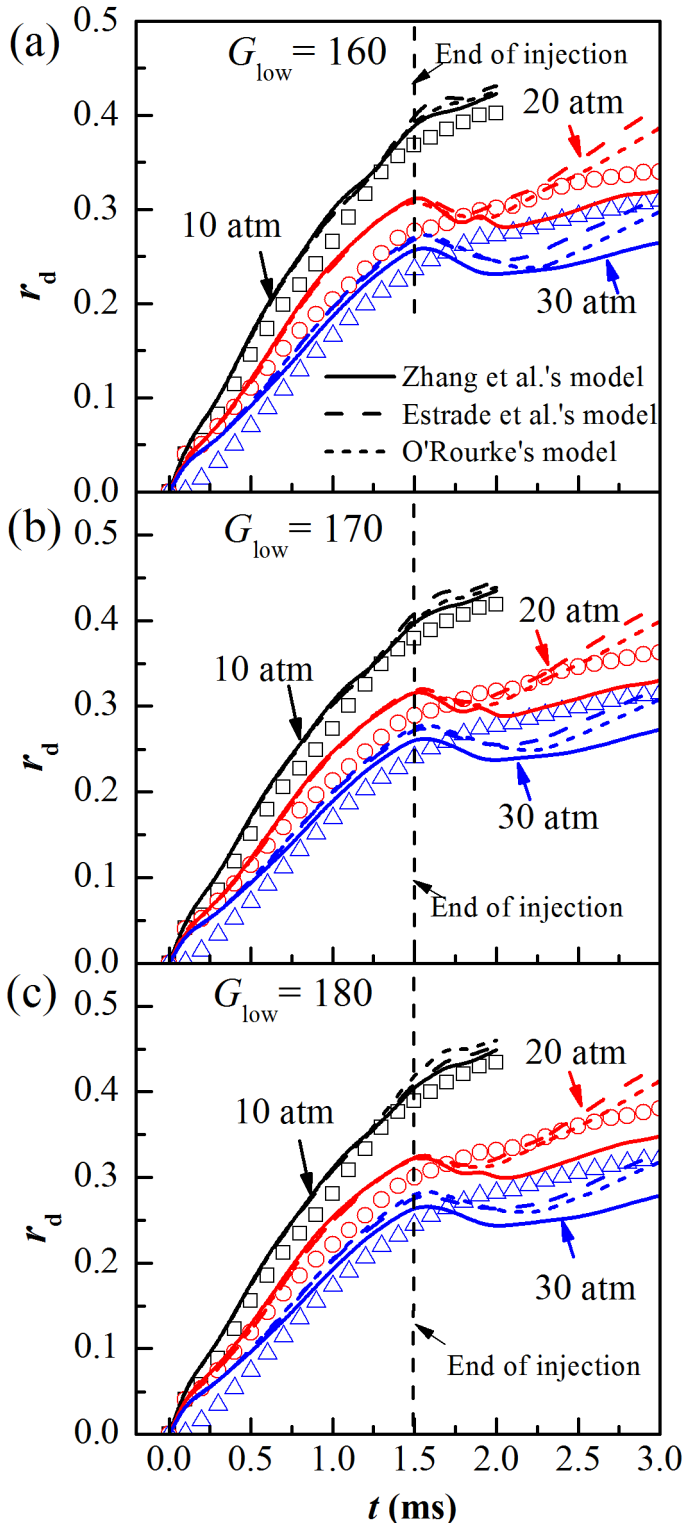

Figure 6. Grayscale level analysis of experimental (denoted by open symbols) and numerical shadowgraph for different thresholds (a) G_{low}=160, (b) G_{low}=170 and (c) G_{low}=180.

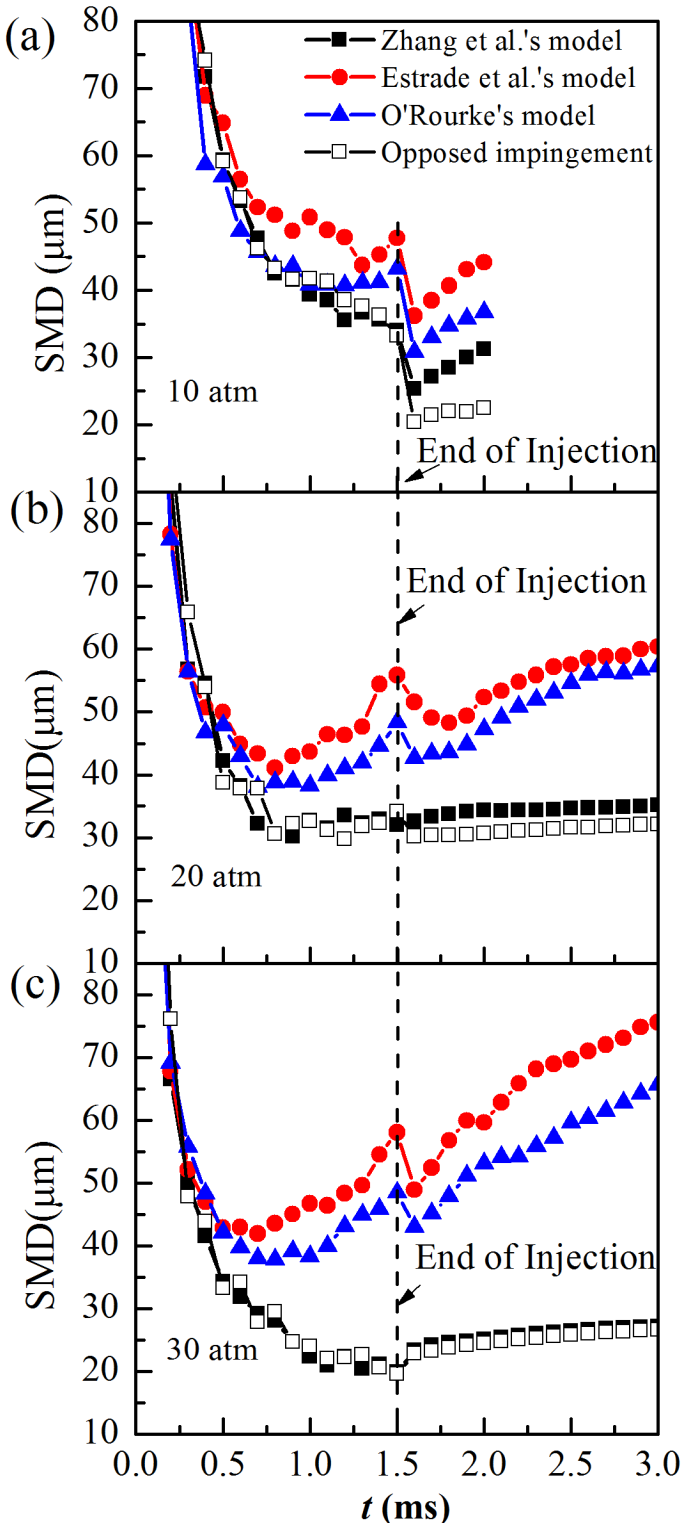

Figure 7. Evolution of predicted SMD in cross-impingement sprays under (a) 10 atm, (b) 20 atm, and (c) 30 atm. SMD in opposed-impingement sprays (Zhang et al., 2016b) [22] are also shown for comparison.

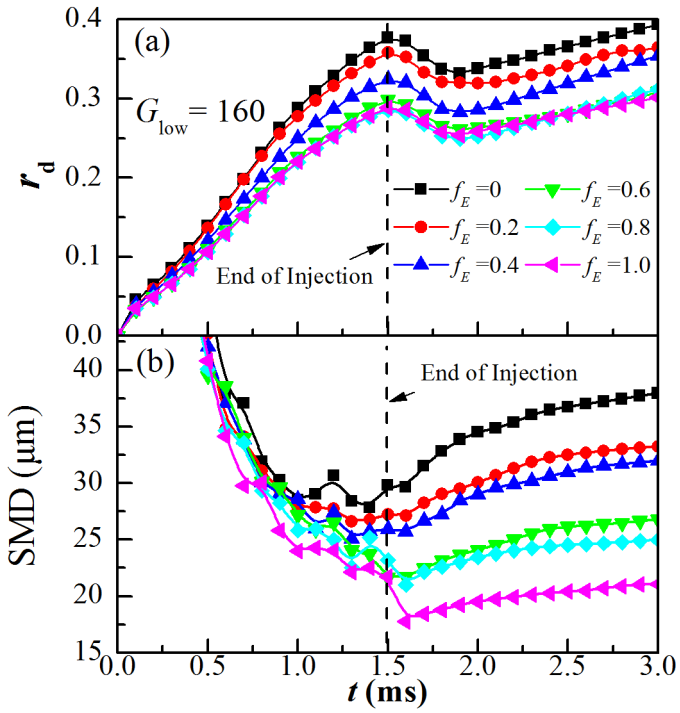

Figure 8. Influence of the uncertainty of kinetic energy recovery factor f_E on (a) r_d and (b) SMD.

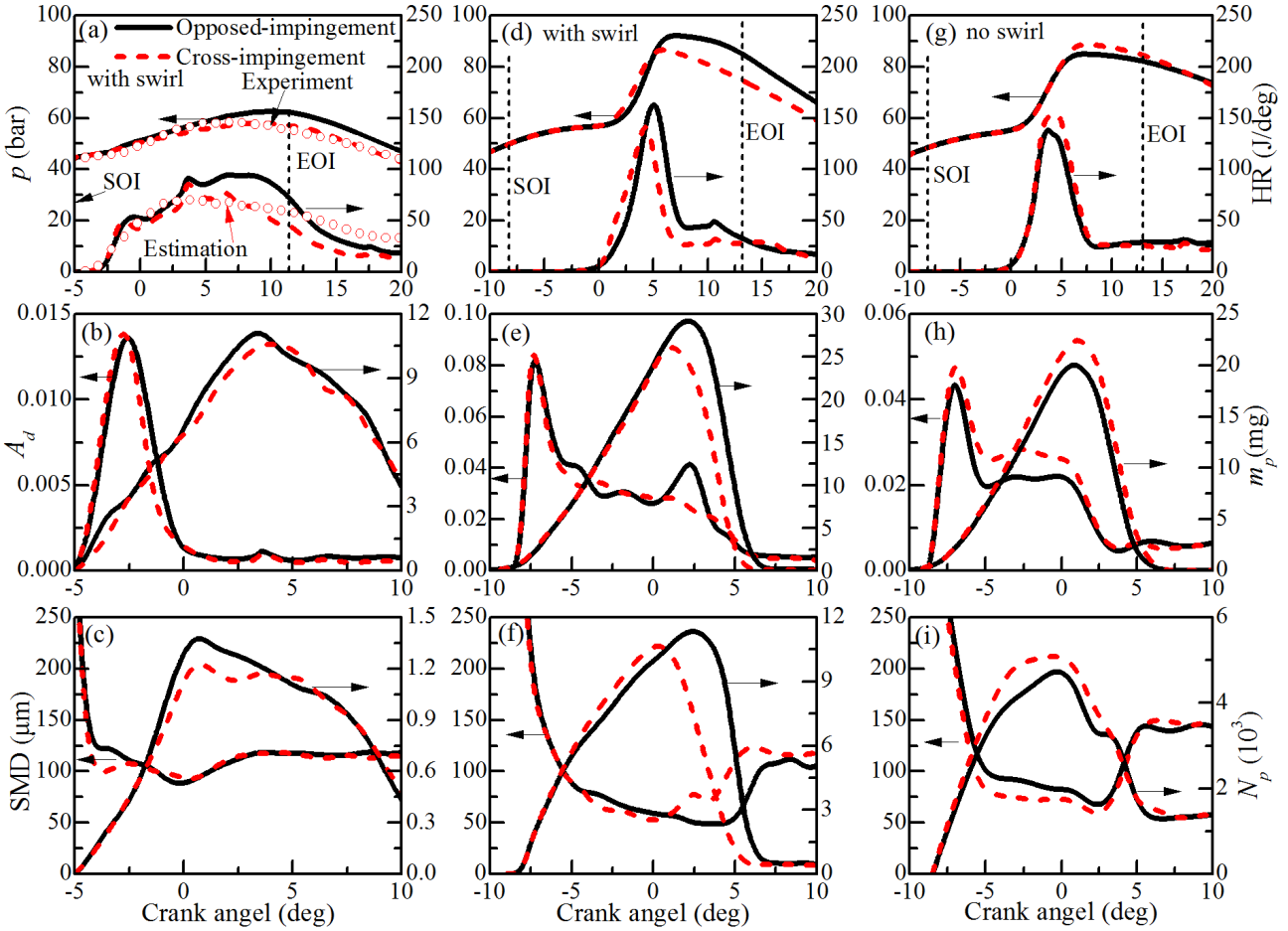

Figure 9. Comparison between spray cross- and opposed-impingement in the model OPCI under the engine speed of 2100 rpm. (a)-(c) 50% load with swirl, (d)-(f) 100% load with swirl, and (g)-(i) 100% load without swirl.

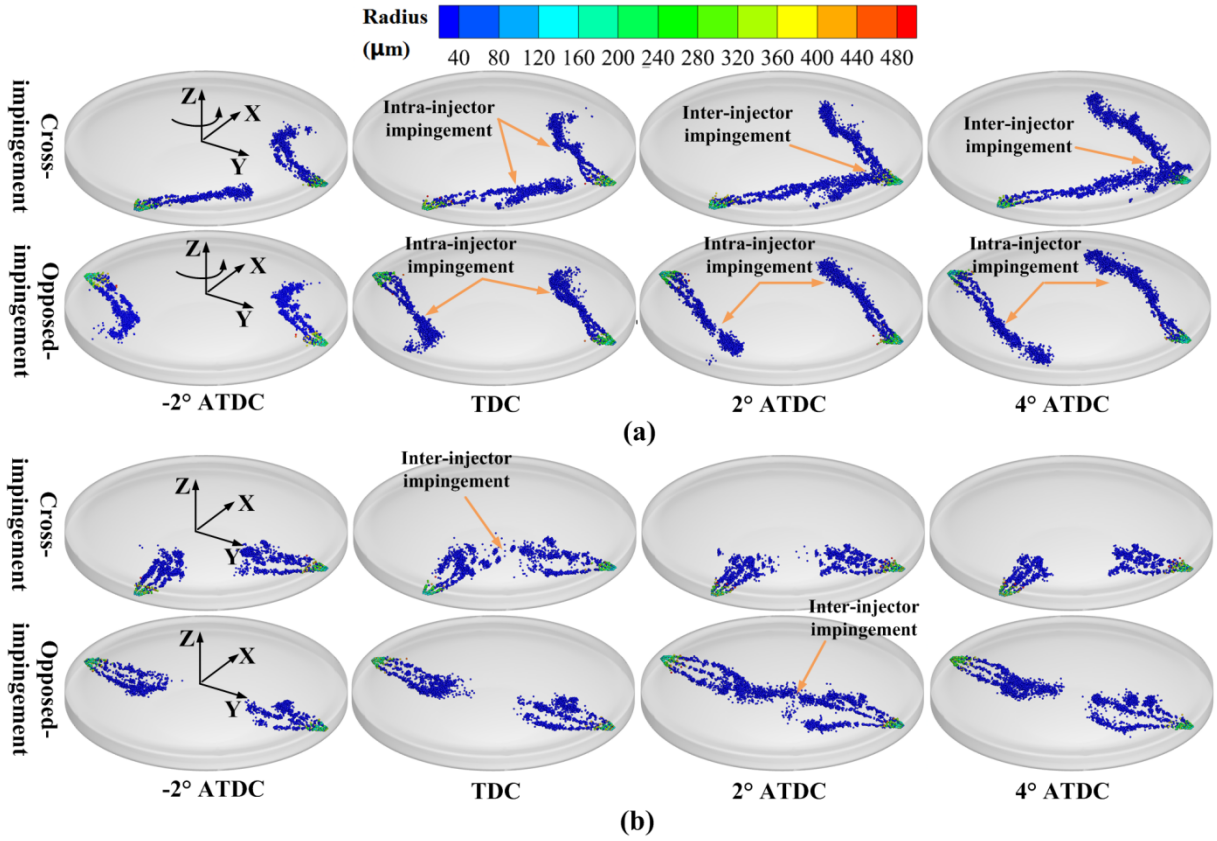

Figure 10. Schematic of intra-injector impingement and inter-impingement under (a) swirling flow and (b) non-swirl flow for spray cross-impingement and opposed-impingement at engine speed of 2100 rpm and 100% load. The shadow in the graphs is the combustion chamber edge.

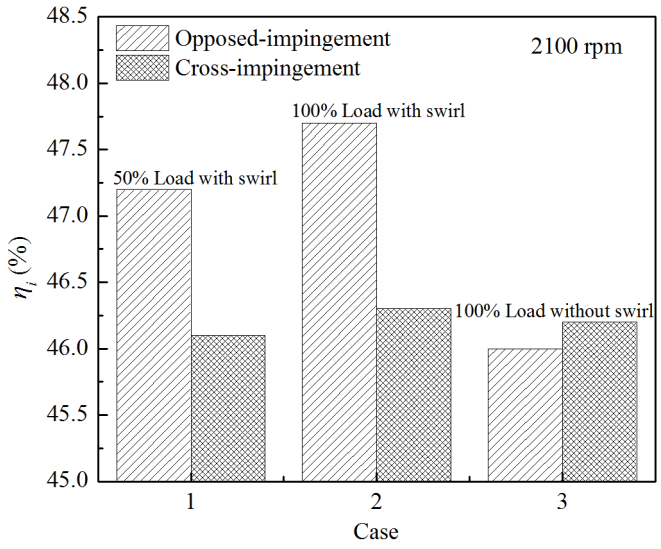

Figure 11. Comparison of engine indicated thermal efficiency η_i between cross- and opposed-impingement under the engine speed of 2100 rpm.

Supplemental Material

Cross-Impingement and Combustion of Sprays in High-Pressure Chamber and Opposed-piston Compression Ignition Engine

Zhenyu Zhang[a], Peng Zhang[a*]

[a] *Department of Mechanical Engineering, The Hong Kong Polytechnic University, Hong Kong, PR. China*

* Corresponding author
E-mail pengzhang.zhang@polyu.edu.hk.
Fax: (852)23654703 Tel: (852)27666664

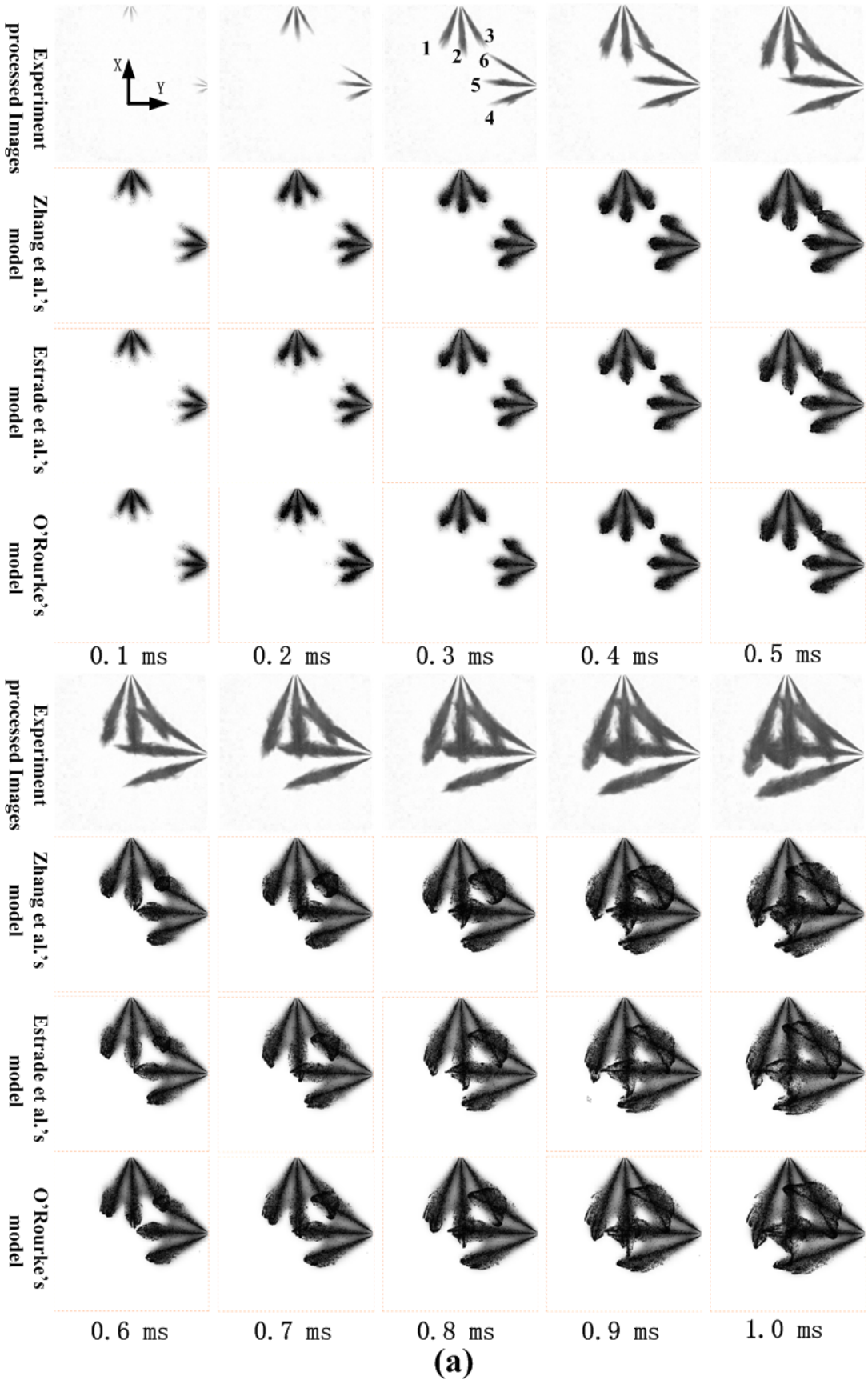
Experiment processed Images
Zhang et al.'s model
Estrade et al.'s model
O'Rourke's model
X
Y
1
2
3
4
5
6
0.1 ms
0.2 ms
0.3 ms
0.4 ms
0.5 ms
0.6 ms
0.7 ms
0.8 ms
0.9 ms
1.0 ms

(a)

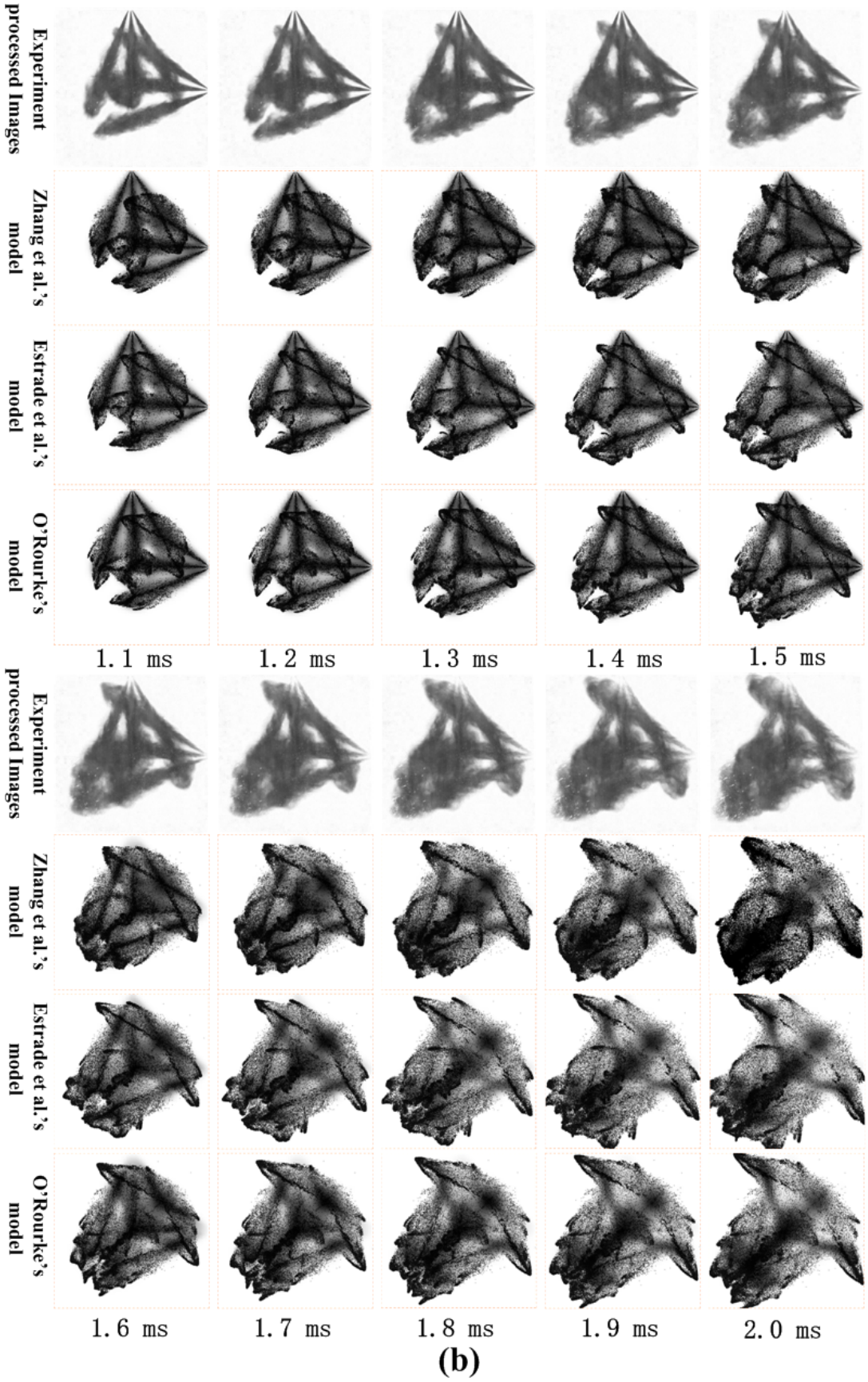

Fig. S1. Experimental and numerical shadwgraph of the spray cross-impingement at 10 atm during (a) 0.1 ms- 1.0 ms and (b) 1.1 ms-2.0 ms. Droplet parcels are also shown in the numerical shadowgraphs.

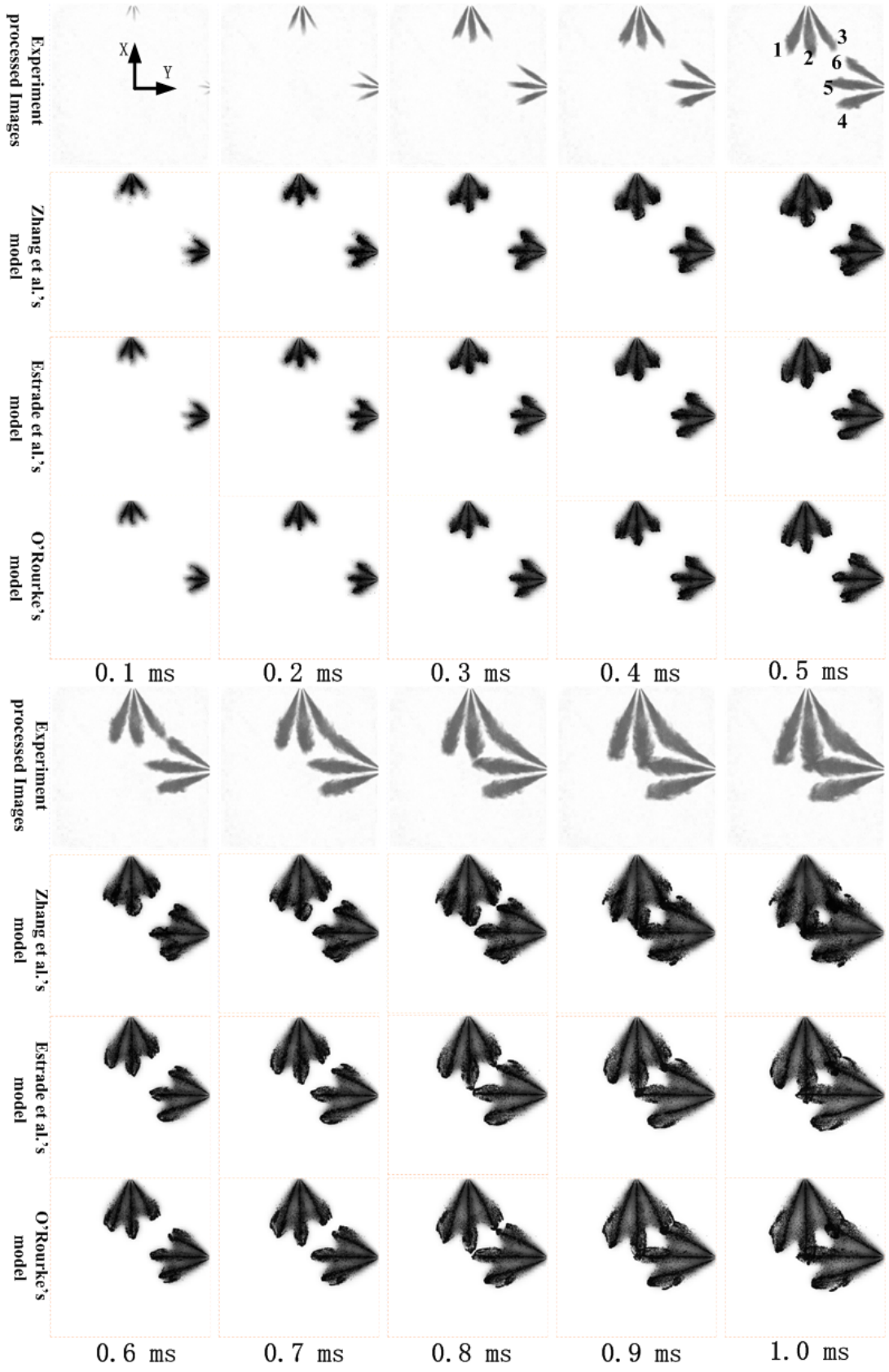
Experiment processed Images
Zhang et al.'s model
Estrade et al.'s model
O'Rourke's model
X
Y
1
2
3
4
5
6
0.1 ms
0.2 ms
0.3 ms
0.4 ms
0.5 ms
0.6 ms
0.7 ms
0.8 ms
0.9 ms
1.0 ms

(a)

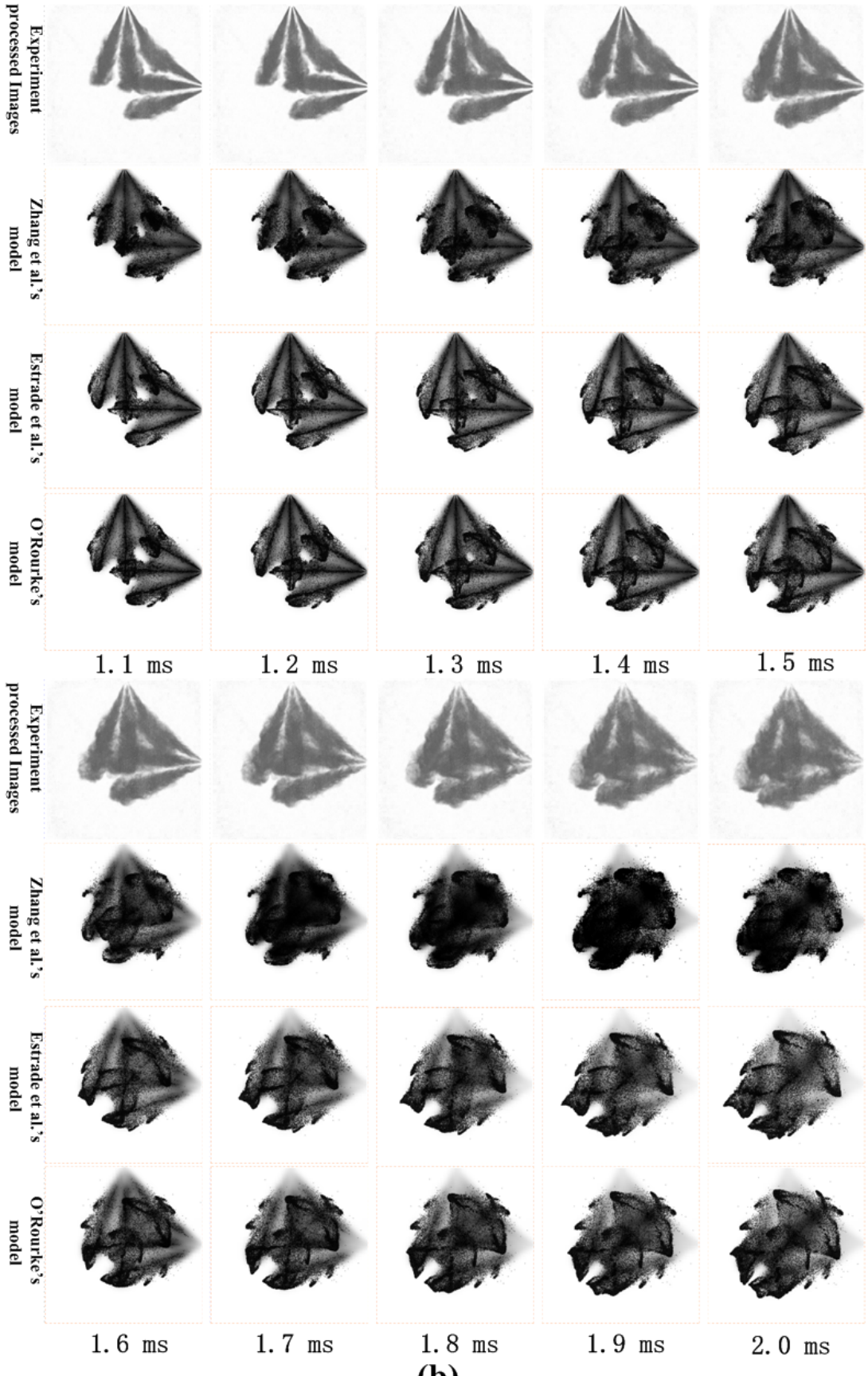
Experiment processed Images
Zhang et al.'s model
Estrade et al.'s model
O'Rourke's model
1.1 ms
1.2 ms
1.3 ms
1.4 ms
1.5 ms
Experiment processed Images
Zhang et al.'s model
Estrade et al.'s model
O'Rourke's model
1.6 ms
1.7 ms
1.8 ms
1.9 ms
2.0 ms

(b)

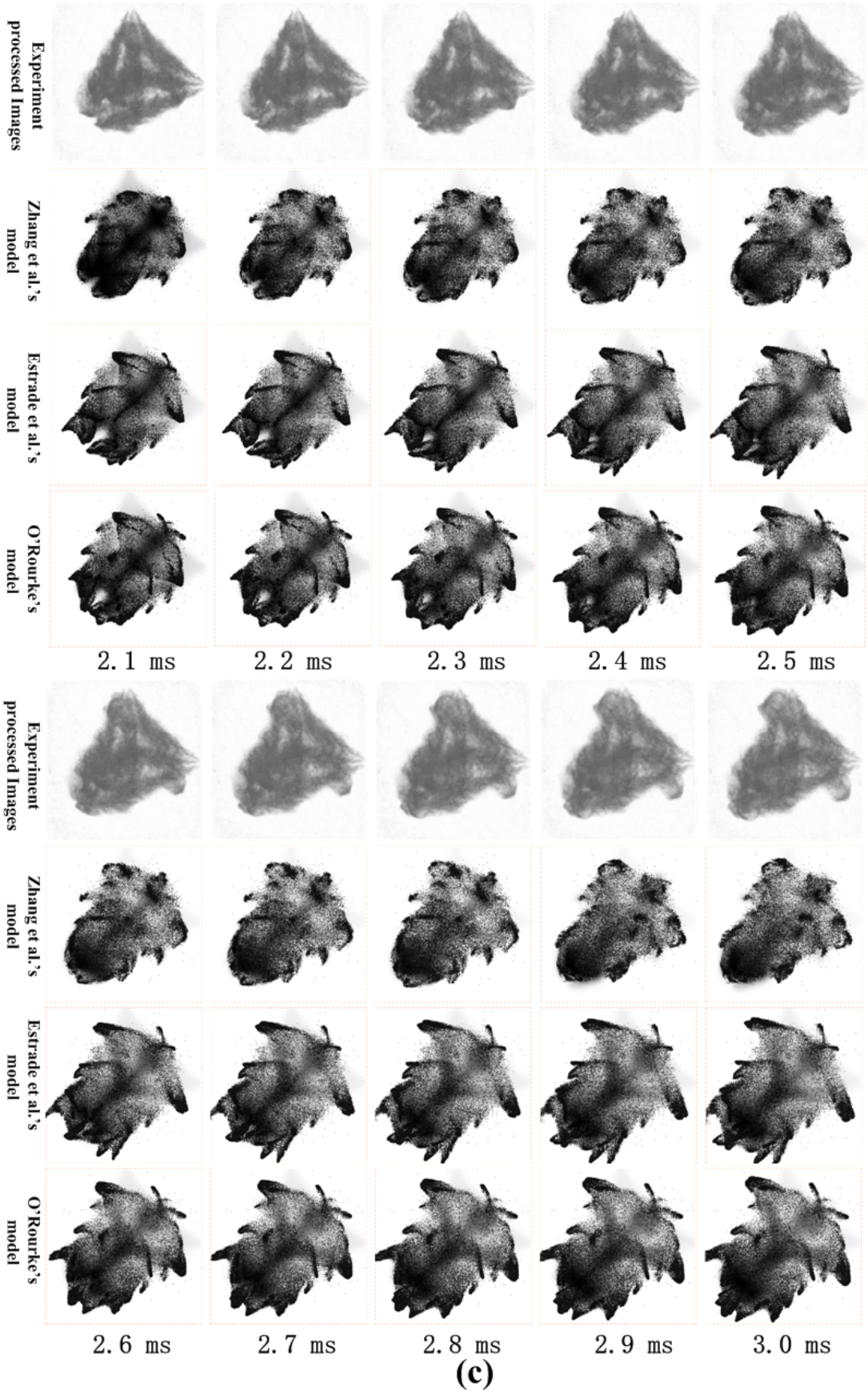

Fig. S2. Experimental and numerical shadwgraph of the spray cross-impingement at 20 atm during (a) 0.1 ms- 1.0 ms, (b) 1.1 ms-2.0 ms and (c) 2.1 ms-3.0 ms. Droplet parcels are also shown in the numerical shadowgraphs.

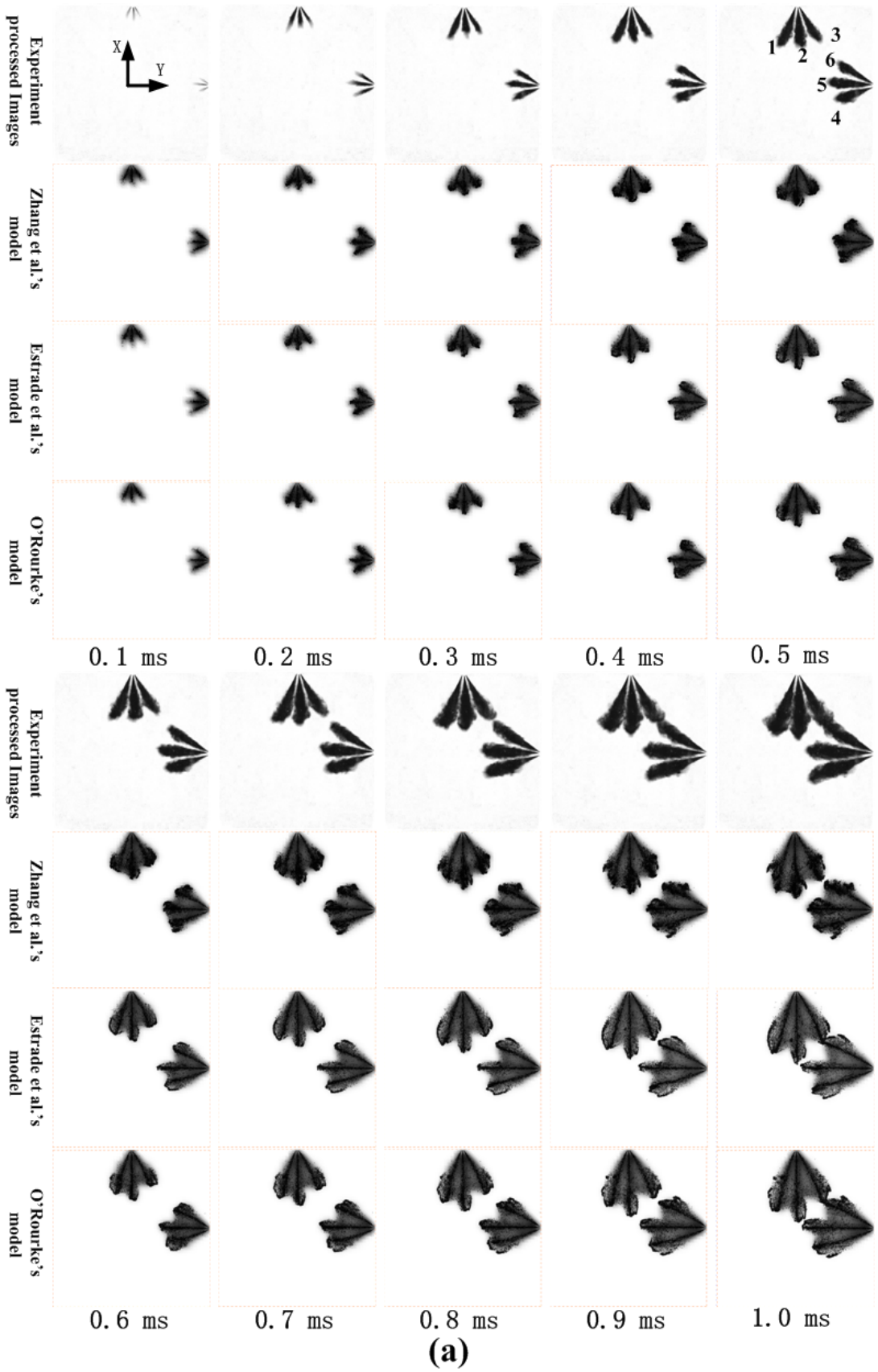
Experiment processed Images
Zhang et al.'s model
Estrade et al.'s model
O'Rourke's model
X
Y
1
2
3
4
5
6
0.1 ms
0.2 ms
0.3 ms
0.4 ms
0.5 ms
0.6 ms
0.7 ms
0.8 ms
0.9 ms
1.0 ms

(a)

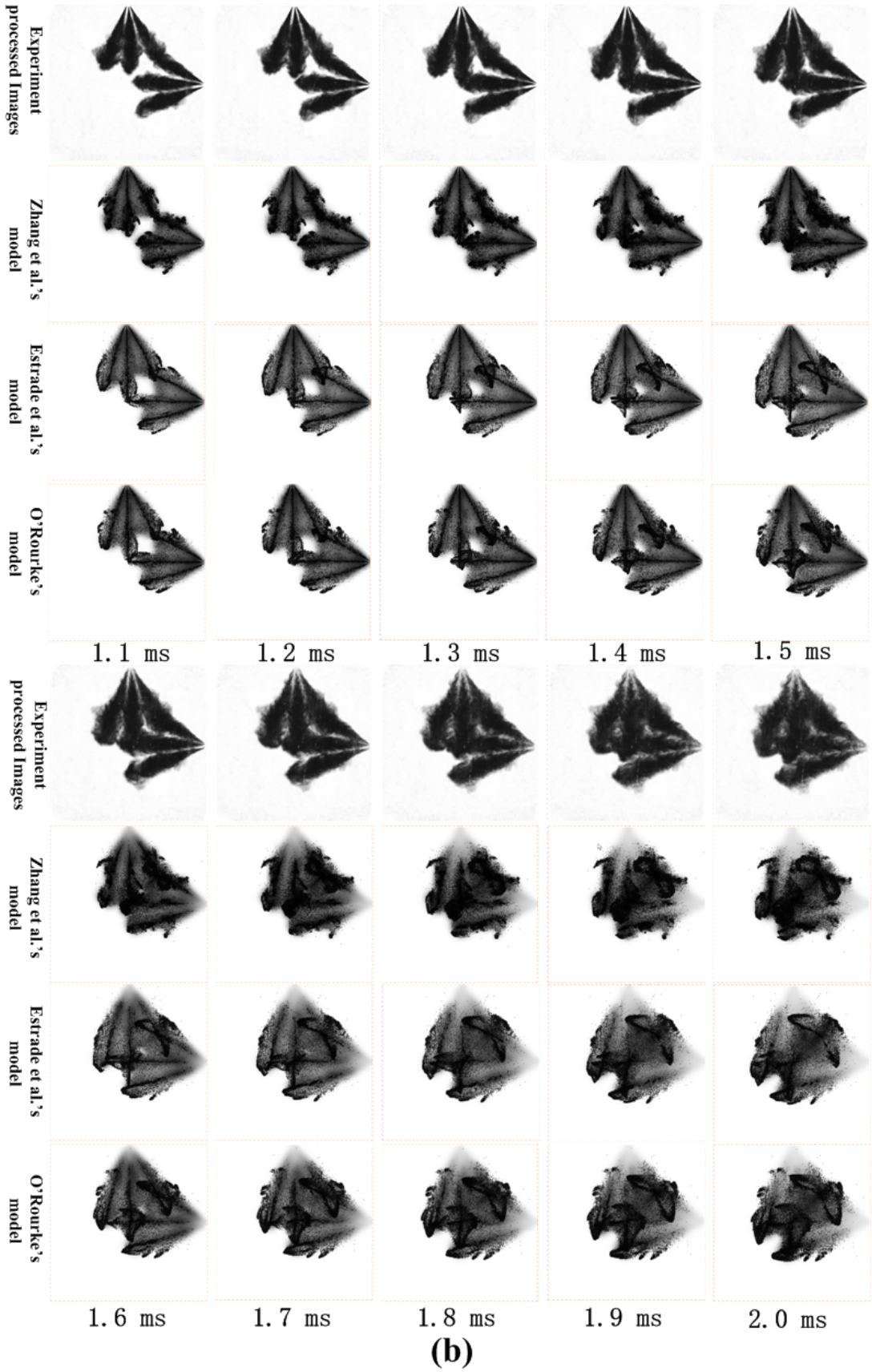
Experiment processed Images
Zhang et al.'s model
Estrade et al.'s model
O'Rourke's model
1.1 ms
1.2 ms
1.3 ms
1.4 ms
1.5 ms
Experiment processed Images
Zhang et al.'s model
Estrade et al.'s model
O'Rourke's model
1.6 ms
1.7 ms
1.8 ms
1.9 ms
2.0 ms

(b)

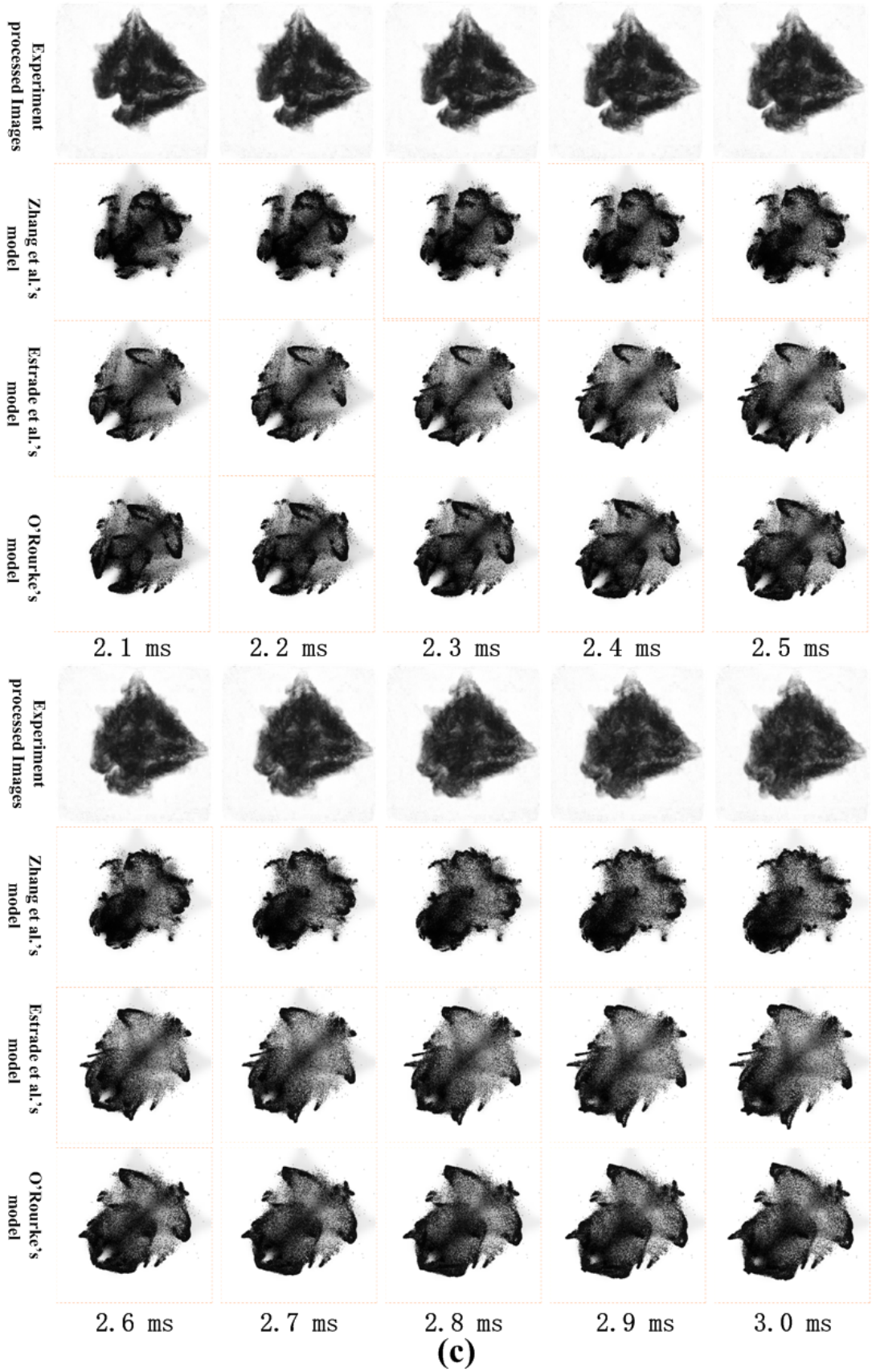

Fig. S3. Experimental and numerical shadwgraph of the spray cross-impingement at 30 atm during (a) 0.1 ms- 1.0 ms, (b) 1.1 ms-2.0 ms and (c) 2.1 ms-3.0 ms. Droplet parcels are also shown in the numerical shadowgraphs.